Title

Hydraulic Modeling of Induced and Propagated Fractures: Analysis of Flow and Pressure Data From Hydromechanical Experiments in the COSC-1 Deep Borehole in Crystalline Rock Near Åre, Sweden

Journal

Water Resources Research, 57(11)

ISSN

0043-1397

Authors

Basirat, Farzad

Tsang, Chin-Fu

Tatomir, Alexandru

et al.

Publication Date

2021-11-01

DOI

10.1029/2020wr029484

AGU ADVANCING EARTH AND SPACE SCIENCE

Water Resources Research

RESEARCH ARTICLE
10.1029/2020WR029484

Key Points:

- Coupled hydromechanical (HM) experiments have been conducted using a step-rate injection method for fracture in-situ properties (SIMFIP) to study fracture generation and propagation in crystalline rock
- Fracture aperture and length can be estimated for successive time stages using simple hydraulic modeling of flow and pressure data from the experiments
- SIMFIP was applied to three borehole sections at about 500 m depth: one without the presence of fracture, one with a no-flow fracture, and one with a flowing fracture. Insight was obtained in their coupled HM behaviors

Supporting Information:

Supporting Information may be found in the online version of this article.

Correspondence to:

F. Basirat,
farzad.basirat@geo.uu.se

Citation:

Basirat, F., Tsang, C.-F., Tatomir, A., Guglielmi, Y., Dobson, P., Cook, P., et al. (2021). Hydraulic modeling of induced and propagated fractures: Analysis of flow and pressure data from hydromechanical experiments in the COSC-1 deep borehole in crystalline rock near Åre, Sweden. *Water Resources Research*, *57*, e2020WR029484. https://doi.org/10.1029/2020WR029484

Received 22 DEC 2020
Accepted 14 OCT 2021

Author Contributions:

Conceptualization: Farzad Basirat, Chin-Fu Tsang

Hydraulic Modeling of Induced and Propagated Fractures: Analysis of Flow and Pressure Data From Hydromechanical Experiments in the COSC-1 Deep Borehole in Crystalline Rock Near Åre, Sweden

Farzad Basirat[1], Chin-Fu Tsang[1,2], Alexandru Tatomir[1], Yves Guglielmi[2], Patrick Dobson[2], Paul Cook[2], Benoit Dessirier[3], Christopher Juhlin[1], and Auli Niemi[1]

[1]Department of Earth Sciences, Uppsala University, Uppsala, Sweden, [2]Lawrence Berkeley National Laboratory, Energy Geosciences Division, Berkeley, CA, USA, [3]Baltic Sea Centre, Stockholm University, Stockholm, Sweden

Abstract To characterize the coupled hydromechanical behavior of rock fractures, the step-rate injection method for fracture in-situ properties (SIMFIP) was conducted with a specialized downhole probe developed by Guglielmi et al. (2014, https://doi.org/10.1007/s00603-013-0517-1). In June 2019, a field campaign was carried out near Åre, Sweden, where the SIMFIP probe was applied in the Collisional Orogeny in the Scandinavian Caledonides-1 scientific borehole to understand the dynamics of injection-induced fracture initiation, fracture opening, and shearing due to water injection-withdrawal in a borehole interval isolated by two packers. Three intervals were investigated at ~500 m depth: (a) an unfractured section (intact rock), (b) a section with non-conductive fractures, and (c) a section with hydraulically conductive fractures. Pressure, injection flow rate, and borehole wall displacement were simultaneously measured during the tests. In the present study, the geometry of the induced fracture and deformation of existing fractures at different time stages of the tests are determined based on a hydrologic model by using the measured pressure and flow data during each time stage of the experiment. A numerical model for the fluid flow within the fracture and the packed-off borehole interval is implemented within COMSOL Multiphysics. By matching model simulations with observed data for all three sections, estimates of the induced and propagated fractures' radius and aperture at successive time stages have been obtained in each case. We could also determine the non-linear relationship between fracture aperture and pressure for values above fracture opening pressures. The model results provide insights for the understanding of pressure-induced fracture initiation and propagation in crystalline rock.

1. Introduction

Fluid flow and transport phenomena through fractured rocks have received significant interest in many geoscience problems such as nuclear and chemical waste disposal, CO_2 sequestration, enhanced geothermal systems (EGS), oil and gas recovery, and unconventional energy resources (Koyama et al., 2008). In hard fractured crystalline rocks, fluid flow occurs through rock fractures due to the inherently low permeability of the rock matrix (Cao et al., 2018; Tsang & Niemi, 2013; Zimmerman & Bodvarsson, 1996). In-situ mechanical and hydraulic processes in fractured rocks are highly coupled (Tsang, 1991; Tsang et al., 2007), and to understand the coupled hydromechanical behavior of fractures, in-situ coupled hydromechanical experiments are needed.

There are a number of in-situ hydromechanical experiments conducted in crystalline rocks, such as experiments performed in the Aspö Hard Rock Laboratory (López-Comino et al., 2017; Zang et al., 2017), the EGS Collab Project in the Sanford Underground Research Facility (SURF) (Guglielmi, Cook, Soom, Schoenball, et al., 2021; Fu et al., 2021), and the underground laboratory of the Grimsel Test Site (Amann et al., 2018; Dutler et al., 2019), which differ from each other in term of monitoring strategies and testing protocol. One of the well-proven protocols to quantify both fracturing and fracture hydromechanical properties is the step-rate injection method for fracture in-situ properties (SIMFIP) (Guglielmi et al., 2014, 2015). Guglielmi et al. (2014) developed a special downhole tool to conduct coupled pressure/deformation transient measurements in packed-off intervals in boreholes subject to flow injection or withdrawal. The method has been applied successfully to characterize and measure deformations in faults and fractures due to water injection

Data curation: Farzad Basirat, Chin-Fu Tsang, Alexandru Tatomir, Yves Guglielmi, Patrick Dobson, Paul Cook, Benoit Dessirier, Christopher Juhlin, Auli Niemi
Formal analysis: Farzad Basirat, Chin-Fu Tsang, Patrick Dobson, Paul Cook, Benoit Dessirier, Auli Niemi
Funding acquisition: Auli Niemi
Investigation: Farzad Basirat, Chin-Fu Tsang, Alexandru Tatomir, Yves Guglielmi, Patrick Dobson, Paul Cook, Benoit Dessirier, Christopher Juhlin, Auli Niemi
Methodology: Farzad Basirat, Chin-Fu Tsang, Alexandru Tatomir, Yves Guglielmi, Patrick Dobson, Paul Cook, Benoit Dessirier, Christopher Juhlin, Auli Niemi
Project Administration: Auli Niemi
Resources: Yves Guglielmi, Patrick Dobson, Christopher Juhlin, Auli Niemi
Supervision: Chin-Fu Tsang, Auli Niemi
Validation: Farzad Basirat
Visualization: Farzad Basirat
Writing – original draft: Farzad Basirat
Writing – review & editing: Chin-Fu Tsang, Alexandru Tatomir, Patrick Dobson, Christopher Juhlin, Auli Niemi

in different underground sites such as in the Low Noise Underground Laboratory (Derode et al., 2015; Duboeuf et al., 2017), the underground research laboratory of Tournemire (De Barros et al., 2016), the Mont Terri Underground Research Laboratory (Guglielmi, Nussbaum, Jenne, et al., 2020; Guglielmi, Nussbaum, Rutquist, et al., 2020), and at SURF (Guglielmi, Cook, Soom, Dobson, et al., 2021; Guglielmi, Cook, Soom, Schoenball, et al., 2021). Since these studies, the SIMFIP tool has been further developed for use in deep slim boreholes, and subsequently, it has been applied to the study of the hydromechanical behavior of fractures in the COSC-1 borehole near Åre, Sweden.

At the COSC-1 borehole, SIMFIP experiments were carried out in three selected borehole intervals around the depth of 500 m (Guglielmi, Chang, et al., 2020; Niemi et al., 2021). The objective was to better understand injection-induced fracture initiation and fracture opening and shearing due to injection-withdrawal of fluid. The tests were conducted in three packed-off sections of about 2-m intervals at ∼500 m depth, containing (a) initially no fracture (an intact rock section), (b) non-conductive fractures, and (c) a zone with several conductive fractures. During the tests, the displacements were continuously measured with an optical fiber-based three-dimensional deformation unit in the SIMFIP probe. The pressure was monitored using a pressure sensor in the packed-off interval, and the injection flow rate was controlled by a pump on the surface. In addition, supplementary borehole data on electrical conductivity, natural gamma ray activity, and temperature data were collected. An overview of the COSC-1 experiment may be found in Niemi et al. (2021), including details on SIMFIP techniques and the injection test itself.

Under the SIMFIP testing procedure, water is injected as pulses into the borehole section being tested, which results in pressure buildup in steps. The injection may be followed by water withdrawal by releasing the wellhead pressure. When the pressure is below a critical value, the process is purely hydrological with the pressure step rise corresponding to injection volume, and the pressure will stay at a constant as a step if the volume of borehole and fractures intercepted by it is limited. However, if the volume is large, or if the fracture is connected to a large flow domain allowing water leakage into it, the pressure will fall slowly after the initial pressure jump with each water injection pulse. For a borehole section without an initial fracture, the injection pressure may reach a large value that will crack the rock, creating a new fracture. This is evidenced by a sudden drop in the pressure data due to the new fracture with its additional volume for water flow. In the case of the borehole section with the presence of a fracture, the injection pressure may be large enough (though less than rock cracking pressure) to overcome confining stresses and open up the existing fracture with an increase in fracture volume, and this is reflected in a relatively slower pressure change as compared with a rigid fracture (pure hydraulic) case. Fracture creation and deformation due to high-pressure injection are coupled hydromechanical (HM) effects. However, if the process is relatively slow, the time sequence may be divided into successive time stages, where, within each time stage, the fracture geometry may be considered to be approximately constant.

The present work aims to identify fracturing and fracture geometry in each of the three test intervals at different time stages of the experiments consistent with the pressure and flow rate data within each time stage by using a simple fracture flow model. This may be considered as an important first step in field data analysis to provide insight into system behavior that would help in further fully coupled hydromechanical modeling analysis. In this first analysis of the experiments, we do not take into account explicitly the mechanical effects in terms of coupled HM modeling. Instead, the mechanical deformation of the rock fractures is accounted for implicitly by varying the fracture aperture and radius from one time stage to the next as the test proceeds. The reason for using this approach is two-fold: First, a simple hydraulic-only approach allows us to examine the main first-order effects and provides insight that could help with further coupled HM modeling studies. Second, there is so far only very limited data and analyses available concerning the site's mechanical properties, especially the local stress field, which would make the results from a coupled HM modeling somewhat uncertain. However, for the sake of comparison and as an example, we have also carried out a fully coupled HM study using reasonable guess parameters for one of the cases, with the objective to verify the consistency between results of the coupled HM model and those of the hydraulic only model. In the following text, we shortly introduce the COSC deep borehole and then the SIMFIP tests with the data acquisition relevant to the modeling, followed by the modeling of fracture flow in these experiments. This is followed by an analysis of the results, discussion, and conclusions.

2. The COSC Deep Borehole

The COSC-1 borehole, located near the town of Åre in western Jämtland, is the first deep borehole for the Collisional Orogeny in the Scandinavian Caledonides (COSC) project to study the structure and physical conditions of the Scandinavian orogenic units within the framework of the International Continental Scientific Drilling Program (Gee et al., 2010; Hedin et al., 2016; Lorenz et al., 2015). The COSC-1 borehole was drilled in 2014 and was subvertical, reaching a depth of 2,495.8 m with nearly 100% core recovery. The borehole diameter is 101.6 mm down to 103 m, 96 mm from 103 m down to 1,600 m, and 76 mm from 1,600 m to the hole bottom at 2,496 m. The borehole intersects a sequence of high-grade metamorphic rocks, such as felsic gneisses, amphibolite gneisses, calc-silicate gneisses, amphibolite, migmatites, and garnet mica schists, with discrete zones of mylonite and microkarst (Lorenz et al., 2015).

One of the objectives of the COSC project is to understand the hydrological characteristics of the geological units and investigate the present groundwater circulation patterns of the mountain belt (Tsang et al., 2016). In this context, flowing fluid electrical conductivity (FFEC) logging (Tsang et al., 1990; Tsang & Doughty, 2003) was applied to the borehole, and three separate downhole tests were conducted to determine the depths of hydraulically conductive features and their transmissivities and salinities. From the analysis of FFEC logging of the COSC-1 borehole, seven hydraulically conducting features (or fractures) were identified between the depths of 200–2,000 m. Respectively, these conductive fractures are located at the depths of 288, 338, 508, 553, 696, 1,214, and 1,243 m (Doughty et al., 2017; Tsang et al., 2016). These depths were slightly adjusted later because of subsequently updated depth calibrations (Dessirier et al., 2021). Two additional conductive fractures were subsequently identified between 2,000 m and the borehole bottom at 2,490 m.

It should be pointed out that the recognized conducting fractures represent only a few percent of the total number of fractures that were observed in downhole televiewer surveying and core samples from COSC-1 (Tsang et al., 2016; Wenning et al., 2017). More specifically, Wenning et al. (2017) identified a total of 249 fractures over the depth of 100–2,000 m in the analysis of image logs of the COSC-1 borehole—in general, these did not include low dipping features located along foliation planes. Most of the identified fractures dip steeply (>70°). The orientation of the fractures is sporadic above ~800 m, which can be explained by scattered near-surface stress, local topographic loading, and glacial loading and unloading. Below 800 m, the orientation of the fractures is more uniform with a tighter distribution primarily oriented with an NW-SE strike. The recovered cores show that many of the fractures are mineralized and are not hydraulically conducting. The identification of seven hydraulically conducting fractures among a total of 249 fractures over this depth range is consistent with the observations of Rhén et al. (2008), Follin (2008), and Follin et al. (2014), who studied fractures in deep crystalline rock in Sweden and came to the conclusion that only 2%–3% of fractures have measurable transmissivity.

3. SIMFIP Test Procedure

The SIMFIP was developed to estimate elastic stiffness (normal and shear), strength (friction coefficient and cohesion), and to measure changes in hydraulic properties (hydraulic aperture and storage) of fractures by making micro-scale elastic and inelastic deformations of a localized fractured rock mass volume (Guglielmi et al., 2014). The instrument used for the injection tests is a SIMFIP borehole probe, which allows for simultaneous measurements of transient fluid pressure and three-dimensional displacements at high frequency or small time steps (Guglielmi et al., 2014, 2015). The SIMFIP probe consists of two inflatable rubber packers to isolate an injection chamber in the open hole, spaced apart at an adjustable distance (in the present work, it was set to 2.41 m). Pressure sensors with a 0.01 MPa accuracy were placed inside and outside of the injection chamber, with an orienting tool (compass) to provide the orientation of measurements, and some downhole valves, tubing, and fiber optic cables. The main part of the SIMFIP probe is a three-dimensional deformation unit for the measurement of deformation in all directions; this unit was set across the fracture and anchored to the borehole wall using clamps that are independent of the packer system. The maximum displacement range of the deformation unit is 0.7 and 3.5 mm in the axial and radial directions of the borehole, respectively, and the minimum detectable measurement displacement range is 5 μm.

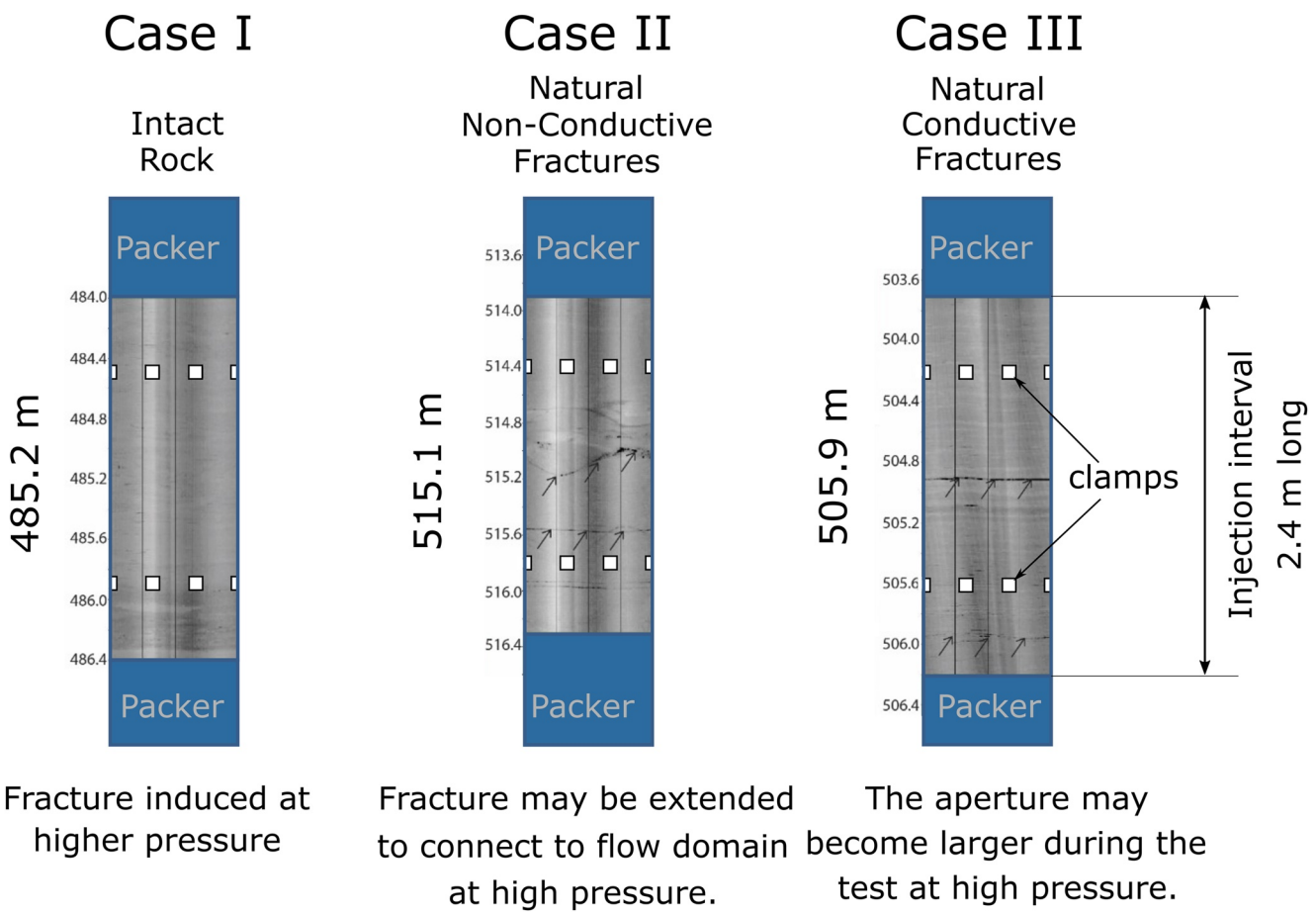

Figure 1. Core televiewer images, along with the locations of the packers and clamps from the step-rate injection method for fracture in-situ properties (SIMFIP) tool for the three intervals at depths of 485.2, 505.9, and 515.1 m studied with the SIMFIP in the Collisional Orogeny in the Scandinavian Caledonides-1 borehole (black arrows show the main geological structures of the intervals).

The SIMFIP tests were conducted at three selected sections in the COSC-1 borehole (Figure 1), and these tests are designated as:

1. Case I, an interval with no initial fracture (intact rock), was chosen between 484 and 486.4 m depth. During the SIMFIP test, a new flat-lying fracture was created at a depth of 484.5 m parallel to the foliation, which was confirmed later by an acoustic image log run after the present series of experiments.
2. Case II, a section with closed or non-conductive fractures between 513.9 and 516.3 m depth. In this interval, one fracture parallel to foliation (260–280/2-13) and the other representing a steeply dipping mineralized fracture (110/59) were observed in the acoustic televiewer log at this section (Figure 1b). In these fractures, no flow was observed in downhole FFEC logging (Doughty et al., 2017). Therefore, the interval is considered as a zone with an initially non-conductive fracture, where the non-conductive property may be due to sealing, aperture closure, or having a dead-end (isolated fracture).
3. Case III, a section with a series of conductive fractures between 503.7 and 506.2 m depth. This zone of conductive fractures was identified by FFEC logging (Tsang et al., 2016), and a subsequent water resistivity measurement indicated flowing fractures at 504.6, 504.8, and 505.9 m, respectively. The fractures are relatively flat, more or less parallel to the foliation with dip direction and dip of 281/5 to 288/12, respectively. No new fractures have been observed in the televiewer images after the tests.

Figure 2 shows the injected flow rate and measured pressure as a function of time during SIMFIP testing in each of the three cases. The test procedure for each section was started by a preliminary test cycle that imposed a step-rate injection at relatively low flow rates (and then pumping out). This cycle (conducted at downhole hydraulic pressures less than 11 MPa) was used to check that no leakage occurs from the packers

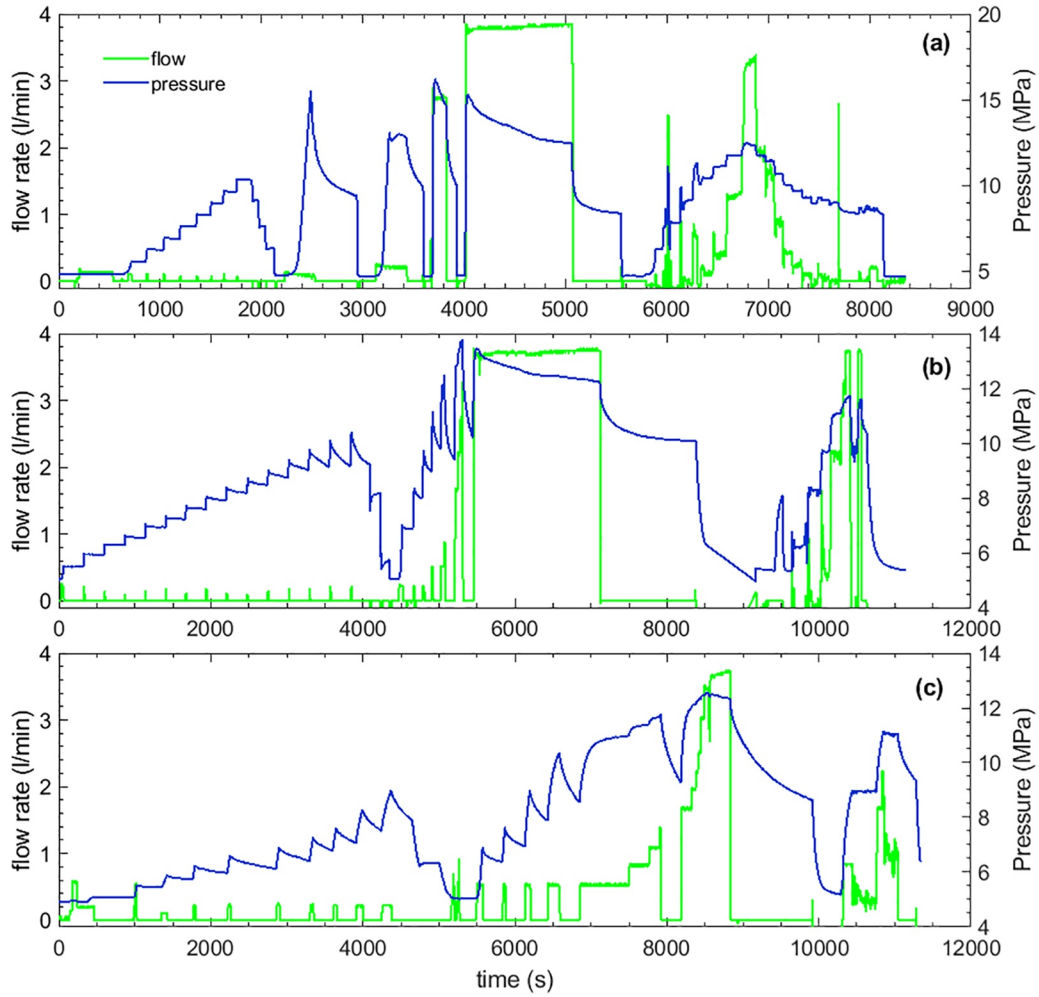

Figure 2. Variation with time of the injected flow rate (left *y*-axes) and pressure (right *y*-axis) in the packed-off section during the step-rate injection method for fracture in-situ properties test in (a) Section with no initial fracture (Case I), (b) Section with non-conductive fracture (Case II), and (c) Section with conductive fractures (Case III).

and to assure the deformation unit clamping efficiency to the borehole wall. After this preliminary cycle, high-pressure stimulation cycles were conducted through a series of injection pulses. The key idea was to create a new fracture in the case of a section initially without fractures or to produce a significant fracture displacement (opening) on an existing fracture. The final cycle was the controlled pressure injection (instead of controlled injection rates) to characterize the fracture's hydraulic properties. In this case, the pressure was maintained constant at different step values by varying the injection flow rate. In the present study, we limited our focus to the analysis of flow and pressure data of the three borehole sections (see Figure 2) in early time periods when the fracturing and/or first fracture propagation/extension occurred. These time periods are 0–3,000, 0–4,100, and 0–4,650 s, respectively, for Cases I, II, and III (see also Figures 4, 5, and 8 below).

4. Conceptual Model and Numerical Simulations

4.1. Hydraulic Modeling

As discussed in the introduction, the main analysis was based on a hydraulic simulation approach where the properties of the generated/propagated fractures were determined at successive time stages based on a detailed matching to the observed pressure and flow during each time stage. Effects of pressure-induced fracture deformation were modeled implicitly by changing the fracture aperture and size from one time

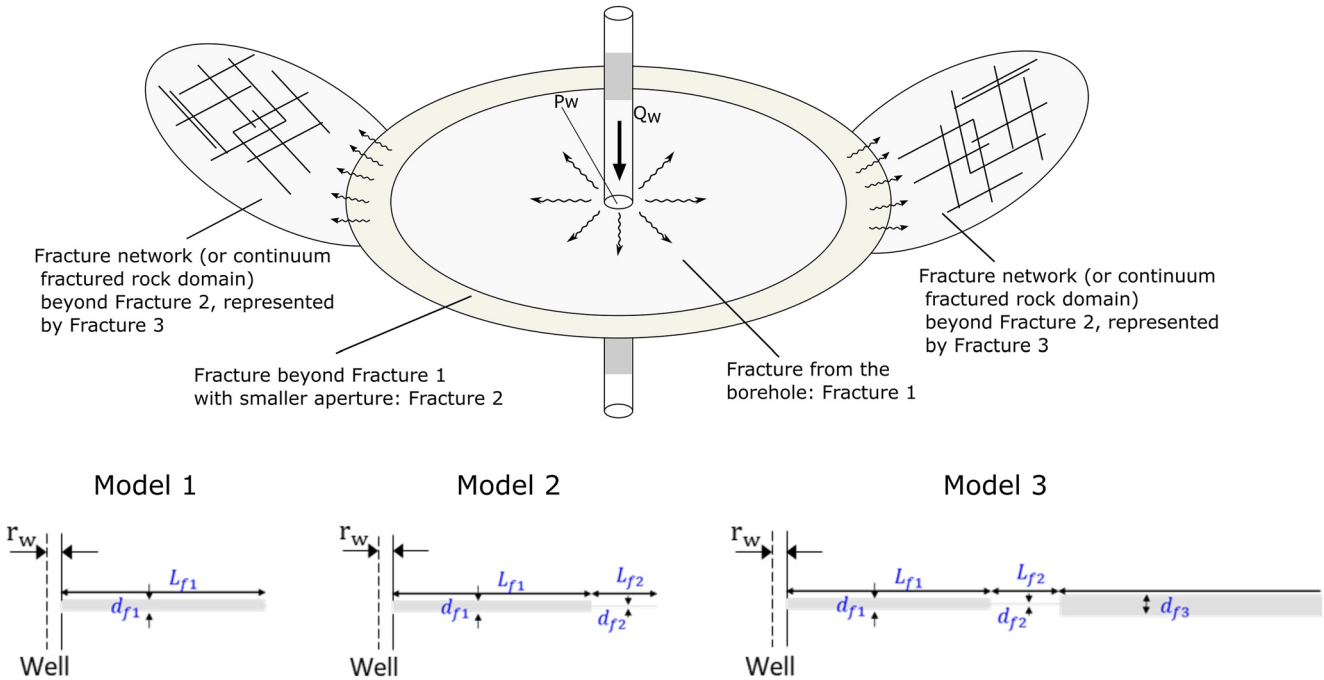

Figure 3. Three conceptual models with a single horizontal fracture with a variable aperture at different radius (adopted from Rutqvist et al., 1998). Model 1 represents a single generated fracture with one aperture, Model 2 is a conceptualization of the fracture ending with a narrower fracture extension region or microcracks, and Model 3 is a conceptualization of the fractures connecting to a further fracture network region.

stage to the next as the test proceeded. The switch from one time stage to the next is made when the data show significant deviation from hydraulic modeling results based on constant fracture parameters. In the absence of additional field measurements and independent data, a simple conceptual model is used to simulate the fluid flow through fractures during the SIMFIP tests. The simplest model which has been found to adequately explain the field data is shown in Figure 3. The model is composed of the main radial fracture (Fracture 1) intercepted by the borehole, and this fracture is connected to the general rock flow domain (represented by Fracture 3) by way of an extension called Fracture 2 (from the radius of the main fracture to a larger radius) having a different aperture. This basic model can be simplified to three alternative conceptual models depicted in Figure 3:

1. Model 1, single fracture (Fracture 1) from the borehole with a constant aperture. As indicated below, the single fracture can also represent several independent fractures intercepted by the borehole (Equation 1). In this Model 1, Fracture 1 has a finite radius with a closed boundary;
2. Model 2, Fracture 1 is connected to a narrow fracture (Fracture 2) which extends from the radius of Fracture 1 to a larger radius. Fracture 2 is assumed to act as microcracks at the end of Fracture 1, that pre-exist (or are formed due to high pressure injection) with Fracture 1. The outer boundary of Fracture 2 is assumed to be closed (no-flow). Fracture 2 can also be interpreted as a narrowing tip region of Fracture 1.
3. Model 3 is similar to Model 2, with additionally Fracture 2 being connected to a continuum fracture domain (or fracture network) represented as Fracture 3. The fracture network (Fracture 3) has higher transmissivity than Fracture 2 and extends to the end of the model domain. This is to account for the possibility that the generated fracture encounters an existing permeable fracture network.

The presented conceptual model as shown in Figure 3 represents the case of several parallel (independent) fractures in the borehole section, with aperture d_i where i represents the fracture number. These fractures can be either pre-existing or induced by high water pressure in the course of the experiment. Assuming the cubic law for fluid flow within fractures (Witherspoon et al., 1980), the d_f in Figure 3 is related to d_i's as follows:

$$d_f = \left(\sum d_i^3\right)^{1/3} \quad (1)$$

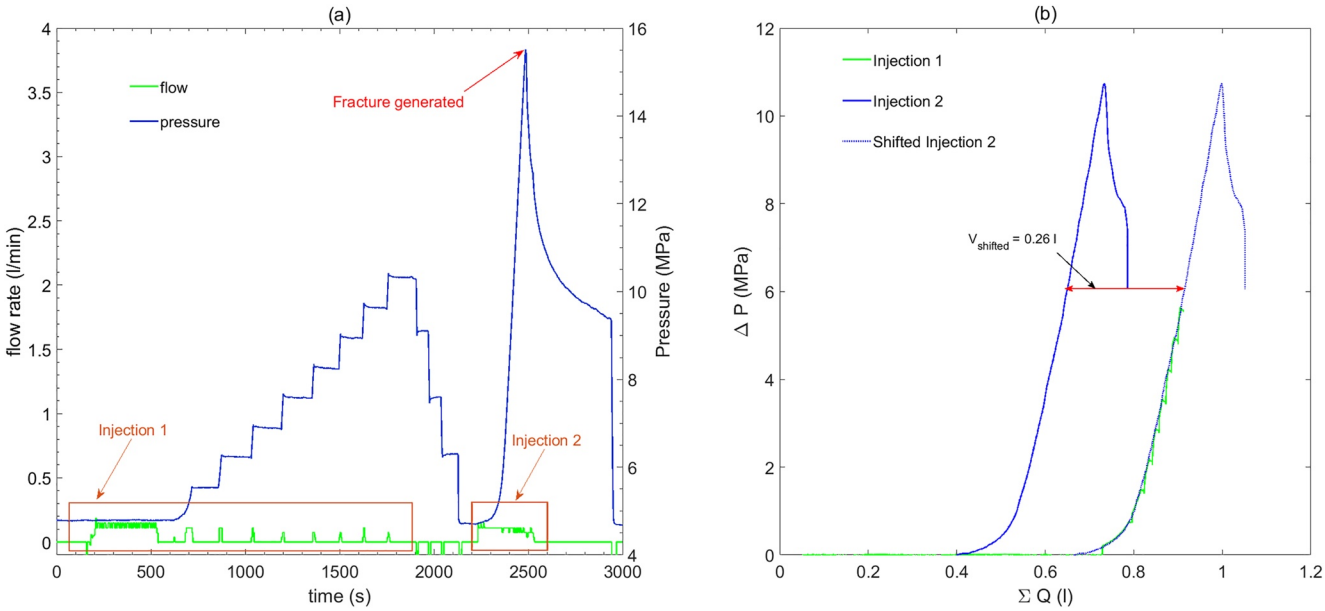

Figure 4. (a) Measured flow rate (left *y*-axes) and pressure (right *y*-axes) as a function of time, up to 3,000 s, and (b) Plot of pressure change versus accumulated injected volume for the two injection stages for step-rate injection method for fracture in-situ properties test in the section with no initial fracture (Case I).

The SIMFIP test sections are simulated as a combined system of the packed-off borehole interval and the series of connected fractures (Models 1, 2, and 3 described above). For each part, the governing equation for fluid flow in porous media based on Darcy's law is applied. The system is regarded as isothermal.

The governing equations were implemented in the commercial computational software COMSOL Multiphysics® 5.4 (COMSOL AB, Stockholm, Sweden; COMSOL Multiphysics® 5.4) based on the finite element method. The numerical implementation of fluid flow in the fracture and porous domains in COMSOL is well established and widely used in different applications. For our particular application, the numerical verification of the model was done against the radial flow model of Theis (1935) for a simple case of a single infinite horizontal fracture. The well-known Theis model is developed for porous medium in an infinite confined aquifer but can be applied to a rock fracture with representative hydraulic conductivity and stor-

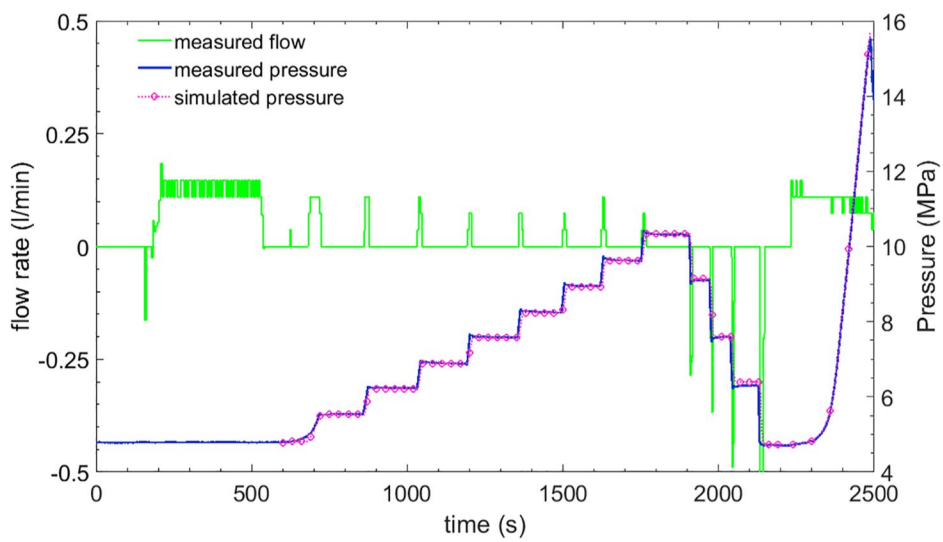

Figure 5. Time of the measured flow rate (left *y*-axis), and modeled and measured pressure for pre-fracturing stages (right *y*-axis).

ativity values as well. The comparison of results showed perfect agreement but is not reported in detail here for space considerations. The conceptual model was constructed and discretized into an axisymmetric model with its center coinciding with the axis of the borehole. The effect of gravity on pressure modeling is small, and therefore, one can assume the fracture is horizontal. The triangular finite element mesh was discretized with extra refinement near the borehole and the fracture and consists of 100,000 elements. In the following, we present the governing equations of the model.

4.1.1. Governing Equations

We used the governing equation for fluid flow in porous media based on Darcy's law for both the fracture models and the borehole section separated by the dual packer system. Because of the low permeability of crystalline rocks and the short duration of the experiment, the flow in the rock matrix domain has been neglected. So, two sets of equations are needed: (a) flow in the fracture and (b) fluid flow in the borehole section, including the effect of the packers, SIMFIP probe, and associated tubing. The latter is the so-called wellbore storage effect which is thus accounted for in the model.

The fluid flow per unit radial length in the Fracture 1, 2, or 3 is modeled as flow between two parallel plates with constant hydraulic aperture (d_f) described by the "cubic law" (Cappa et al., 2008; Witherspoon et al., 1980):

$$q_f = \frac{d_f^3}{12\mu}\left(\nabla_T p + \rho g \nabla_T h\right) \tag{2}$$

where q_f is the flow rate per unit width of the fracture, ρ is the fluid density, g is the gravitational acceleration, μ is the fluid dynamic viscosity, d_f is the hydraulic aperture, and p is pressure, h is the vertical coordinate, and ∇_T denotes the gradient operator restricted to the fracture's tangential plane. The equation of fluid flow in the fracture, in combination with the continuity equation integrated over the fracture cross-section, becomes a single equation with pressure as the only variable:

$$d_f \frac{\partial}{\partial t}\left(\varepsilon_f \rho\right) + \nabla_T \cdot \left(\rho q_f\right) = d_f Q_m \tag{3}$$

where ε_f is the fracture porosity, and Q_m is the mass source term.

In terms of hydraulic concepts, the storativity (S) expresses the unit change in the weight of fluid stored per unit area of a fracture in response to a unit increase in pressure and is defined according to Domenico and Schwartz (1998):

$$S = \frac{1}{A}\frac{\partial\left(\rho g V_f\right)}{\partial p} \tag{4}$$

where A is the area of the fracture plane, p is the fluid pressure, and V_f is the fluid volume between two fracture faces. By applying the chain rule to the above equation, the term S (storativity) is dependent on fluid compressibility and a structural compressibility component:

$$S = \rho g\left(d_f \mathrm{X}_f + \frac{\partial d_f}{\partial p}\right) \tag{5}$$

where d_f is the void aperture, that is the accessible volume contained per unit area of fracture (Rutqvist et al., 1998), and the X_f is the compressibility of the fluid. The void aperture should include both the open space between the fracture surfaces and the storage provided by the porous fracture filling (Rutqvist et al., 1998). The second term of the above equation represents the result of volume increase due to fracture opening as the fluid pressure increases during an injection test. In the present study, the parameter of fractured rock storativity is assumed to be equal to 1×10^{-8}, based on the estimation of storativity in granitic rock at similar depths by Rutqvist et al. (1998). Further details on storativity effects on modeling results are discussed in Section 5.4. The fluid flow equation with fracture storativity takes a slightly different form when compared with Equation 1:

$$S_f d_f \rho \frac{\partial p}{\partial t} - \nabla_T \cdot \left(\rho q_f\right) = d_f Q_m \tag{6}$$

In this equation, S_f is the fracture storage coefficient (storage capacity) with unit 1/Pa and can be defined as:

$$S_f = \frac{S}{\rho g d_f} \tag{7}$$

The equations for the wellbore are in the general form of fluid flow in porous media:

$$\boldsymbol{u} = -\frac{K}{\mu}\left(\nabla p + \rho g \nabla h\right) \tag{8}$$

$$\frac{\partial}{\partial t}\left(\varepsilon_w \rho\right) + \nabla \cdot \left(\rho \boldsymbol{u}\right) = Q_m \tag{9}$$

$$\frac{\partial}{\partial t}\left(\varepsilon_w \rho\right) = \rho S_w \frac{\partial p}{\partial t} \tag{10}$$

where ε_w is the effective "porosity" of the wellbore section, and the S_w is the storage coefficient of the wellbore section (including tubing, probe, and packers).

Due to the choice of the conceptual model, a 2D radial axisymmetric model is used. The model consists of the borehole flow domain of 241 × 5 cm interfaced with the impermeable rock domain of 241 cm × 100 m and a one-dimensional (radial) fracture at the center (see Figure 3). The top and bottom boundary conditions of the model are assumed to be no-flow with 241 cm space between them, corresponding to the borehole section isolated by the two inflatable packers. The outer boundary of the model is placed at 100 m, sufficiently far from the wellbore, so that it does not affect the results over the time of the experiment. The outer boundary of the fracture is assumed to be constant pressure. The water inlet is represented by imposing a Neumann boundary condition at the top of the borehole domain, and its rate is equal to the measured injection flow rate in each test. In addition, it is assumed the wellbore skin effect is negligible, which was confirmed in post-test televiewer logging that showed no damage in the wellbore.

4.2. Coupled Hydromechanical Analysis

As a supplement to our main analysis and for comparison with results from the above hydraulic model, a simple coupled hydromechanical model was also developed and applied to one example, which is Case I on data for the time period after the fracture has been generated up to 3,000 s (which is the focus of data analysis in the present study). The governing equations describing the coupled HM processes follow the implementation of Zhou et al. (2021), and it was also implemented in COMSOL Multiphysics. The simulation model is made similar to the hydraulic model but implemented for the HM context, with reasonable input data of mechanical parameters and boundary conditions, which are mostly unavailable specifically for the site at the tested locations. The numerical model and model design are presented in the Appendix A.

A parameter of specific interest when comparing the hydraulic-only simulation with the coupled HM model is storativity, which is related to the deformation and depends on normal fracture stiffness. A relationship between the normal fracture stiffness and storativity (noted as S_f) can be expressed according to Rutqvist et al. (1998):

$$S_f = \rho \mathbf{g}\left(X_f d_f + \frac{1}{k_n}\right) \tag{11}$$

where k_n is the normal fracture stiffness.

A series of sensitivity analyses were conducted with regard to the key hydromechanical parameters, that is, fracture aperture and the related parameter of fracture permeability, elastic moduli of the rock, and the fracture normal stiffness. Further, as the HM model requires an estimation of the initial stress field, we also perform a sensitivity analysis concerning the horizontal $\left(\sigma_1\right)$ and vertical stresses $\left(\sigma_3\right)$, starting from the

rough estimation provided by Guglielmi, Cook, Soom, Dobson, et al. (2021). These sensitivity analyses are performed by applying the one-at-a-time method, which starts with a base case and then calculates changes by modifying one parameter at a time within a reasonable range. The results are discussed in Section 5.5.

5. Simulations and Results

Sections 5.1–5.4 present results from the main approach using the hydraulic model and Section 5.5 presents results from the supplementary coupled hydromechanical model for one case for comparison purposes.

5.1. Study of the Section With No Initial Fracture (Case I)

The pressure and flow rate data from the SIMFIP test on the section at 485.2 m depth are presented in Figure 2a. The test was initiated with a low imposed pressure step rate test up to 1,905 s. At this stage, water was injected in eight pulses, with a short duration of about 20–30 s and with low flow rates (about 0.1 l/min) into the packed-off section. The pressure data show a constant step-wise increase at each injection pulse, after the first injection step that mainly pressurized the pipes and the packed-off section with water. At the end of this first stage (t = 1,886 s), which we call Injection 1, water was released from the packed-off section to return to the hydrostatic condition for the next stage. The next water injection (Injection 2) was a continuous injection from 2,233 to 2,533 s at a constant flow rate of 0.1 l/min. During this time period, a fracture was induced at 2,487 s when the pressure reached 15.5 MPa. At that point, the pressure is found to drop even as the injection continued because of the induced fracture (Figure 4a). The pressure then gradually decreased until it reached 9.5 MPa at 2,940 s, when another water release is done. In the next sections, we present first the analysis of pressure and flow rate data for pre-fracturing stages in order to calculate the packed-off section storativity. Then, the analyses of the induced fracture using the proposed conceptual models (Figure 3) are presented for data up to the time of 3,000 s.

5.1.1. Analysis of the Pre-Fracturing Stage

The interpretation of the pre-fracturing pressure records is required for the calculation of effective storativity (storage capacity) of the wellbore section (including the tubing, the probe, and the packer system). The wellbore storativity is dependent on the relation between the accumulated injection volume and the pressure change (the measured pressure against the hydrostatic pressure in the packed-off section). Figure 4b shows the accumulative flow rate versus pressure change for the two stages of the injection before the fracture is induced. The slope of these curves represents the storage capacity of the section (without fracture). The curves for both injections have the same slopes, which means that the storage capacity of the borehole section remains almost unchanged for the two injection stages (Figure 4b). However, there is a fixed difference between the accumulated injection volume of Injection 1 and Injection 2 at any pressure. This difference in injected volumes can be explained by the amount of water first needed to fill the tubes and the packed-off section before the pressure starts to increase. By adding 0.26 l to the total injection volume of Injection 2, the curve shifts to the right, and the two curves generally overlap each other. This suggests that the wellbore storativity remains unchanged during the two injections. Note that no leak-off can be seen in these curves because of the low permeability of the rock matrix and the sealing of the injection interval in the borehole by two inflatable packers. In addition, the shape of the two curves suggests that the wellbore storage capacity has a non-linear relationship to the total injection volume. However, this non-linearity vanishes at higher pressures (Figure 4b).

The simulated and measured pressure evolution for the pre-fracturing stage is shown in Figure 5. The modeling is conducted in two steps. In the first step, the step-rate water injection (Injection 1) from 600 to 1,800 s is modeled. This model is used to determine the term V_b representing the bulk volume (including volume between packers, the probe, tubing and etc.) in the equation of storativity (Equation 9). The modeled pressure with parameter V_b equal to 18.9 l shows a very good match with the measured pressure data. In the second step, the calibrated wellbore storativity function is used, and it shows very good agreement with measured pressure for Injection 2 (from 2,200 to 2,486 s). The wellbore storativity function determined here is used in all subsequent simulations when modeling all three cases, as presented below.

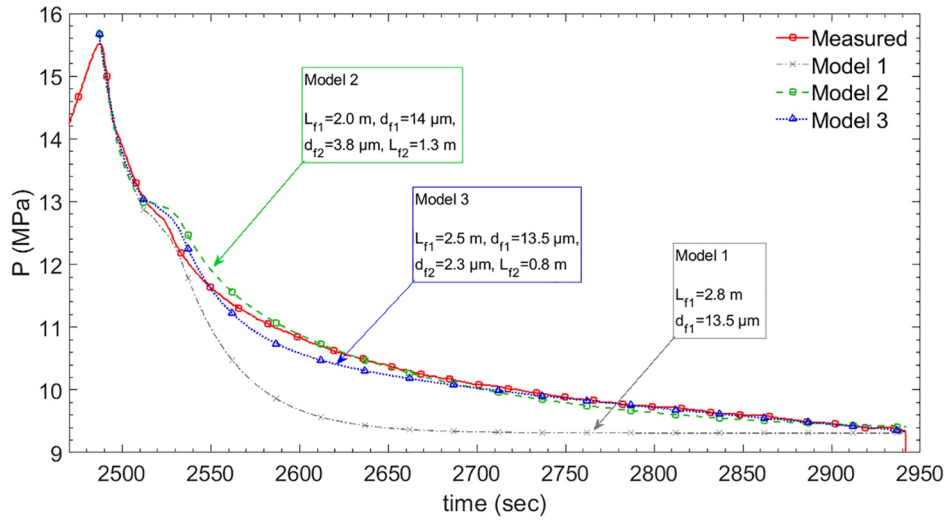

Figure 6. Time of the measured and the simulated pressures of the three conceptual models (See Figure 3).

5.1.2. Analysis of Induced Fracture Stage

In the next stage of the test, the pressure was further increased in steps with injection pulses. At 2,486 s a sudden drop in pressure is observed, implying that a fracture has been induced in the hard rock (Figure 6). The fracturing pressure is found to be about 15.5 MPa, which is related to the tensile strength of the rock. Three conceptual models of the induced fracture (Figure 3) are used to model the observed pressure behavior after fracture creation. The results that best match the field data for each model are shown in Figure 6 along with the measured pressure. The conceptual model 1 represents a closed fracture with a constant aperture and the best match was obtained with a fracture radius of $L_{f1} = 2.8$ m and a fracture aperture d_{f1} of 13.5 μm. The aperture of the fracture controls the early pressure decrease just after the fracture was created and before the injection was ended. An increase of the aperture value would result in a larger pressure reduction and an increase in fracture radius value would result in a larger decrease in pressure at the end of this stage. The pressure from Model 1 shows very good agreement with measured pressure for early and late times, but, for the time in between, the modeled and measured pressures are very different.

On the other hand, the simulated pressures from conceptual models 2 and 3 (See Figure 3) with a small aperture at the far end of the induced fracture are found to match much better with the measured pressures (Figure 6). Model 2 consists of (a) an induced fracture from the borehole (f_1) and (b) a second fracture beyond fracture 1 with a smaller aperture (f_2). The best result for Model 2 is for the fracture radius L_{f1} and L_{f2} of 2.0 and 1.3 m, with the respective fracture apertures d_{f1} and d_{f2} of 14.0 and 3.8 μm. Model 3 is different from Model 2 in terms of the outer boundary of the second fracture (f_2). In Model 2, the second fracture ends with a closed boundary, while in Model 3, the second fracture is open to a fracture network (or continuum fractured rock), represented by f_3. The best result for Model 3 is for the fracture radius L_{f1} and L_{f2} of 2.5 and 0.8 m, respectively, and with the fracture apertures d_{f1} and d_{f2} of 13.5 and 2.3 μm. The aperture of the fracture network beyond the second fracture d_{f3} is 100 μm and the results turn out to be not very sensitive to the value of this parameter. Both Models 2 and 3 provide a good match with the measured pressure before the injection was ended at 2,520 s. But, during the remaining part of the test, Model 3 shows better agreement. In all three conceptual models, the estimated apertures of the fracture at the borehole are in the same range (13.5–14 μm). Also, the total radius of the two fractures in both models is 3.3 m. The corresponding volume of fractures for Model 2 is equal to 0.26 l and for Model 3 is 0.30 l. After some consideration, Model 3 is selected to represent Case I, because of the good match between data and model results and also because the same model can be used for the analyses of Case II and Case III data, see below. Thus Model three is used consistently for all data analyses in this paper.

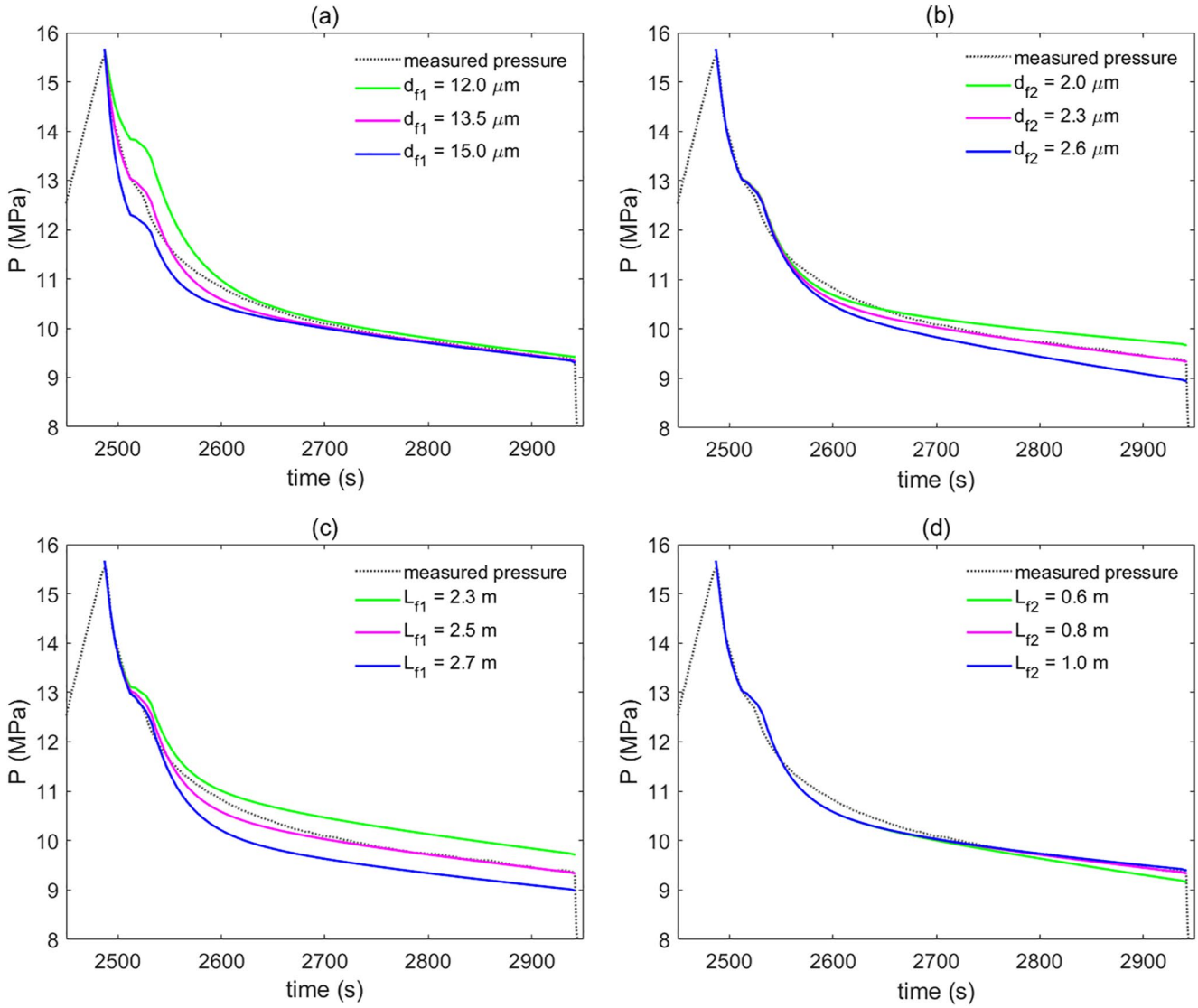

Figure 7. Effect of changes in conceptual Model 3 parameters on pressure variation with time, (a) Aperture of Fracture 1 (d_{f1}), (b) Aperture of Fracture 2 (d_{f2}), (c) Radius of Fracture 1 (L_{f1}), and (d) Radius of Fracture 2 (L_{f2}). Experimental data from Case I are given for comparison (black dotted line).

5.1.3. Sensitivity Analysis of Induced Fracture Parameters

To understand the effect of the different fracture parameters on the calculated pressure response, sensitivity analyses of each parameter is carried out individually with Model 3 (Figure 7). For each sensitivity analysis, one lower value and one higher value than the best matching value for each parameter were used. The main fracture aperture (d_{f1}) affects the pressure before injection ends (Figure 7a) but does not significantly affect the pressure during the remainder of the test. The result shows that an 11.1% increase of d_{f1} value can increase the pressure drop by approximately 5.5% for the time before the injection is stopped (Figure 7a). In contrast, an 11.1% decrease of d_{f1} values can reduce the pressure drop by about 6% for the same time period. Unlike d_{f1}, the aperture of Fracture 2 (d_{f2}) has the main effect on the pressure after the injection ends. A 13% increase of d_{f2} value results in a pressure reduction of 4% at the end of this stage. In contrast, a 13% decrease of d_{f2} value results in a pressure increase of 4% (Figure 7b). The increase of Fracture 1 radius value (L_{f1}) reduces the pressure immediately after the injection ends (Figure 7c). The effect of the radius of Fracture 2 (L_{f2}) on pressure is not very significant. An increase of L_{f2} causes a smaller pressure drop mainly at the end of this stage at 2,940 s (Figure 7d).

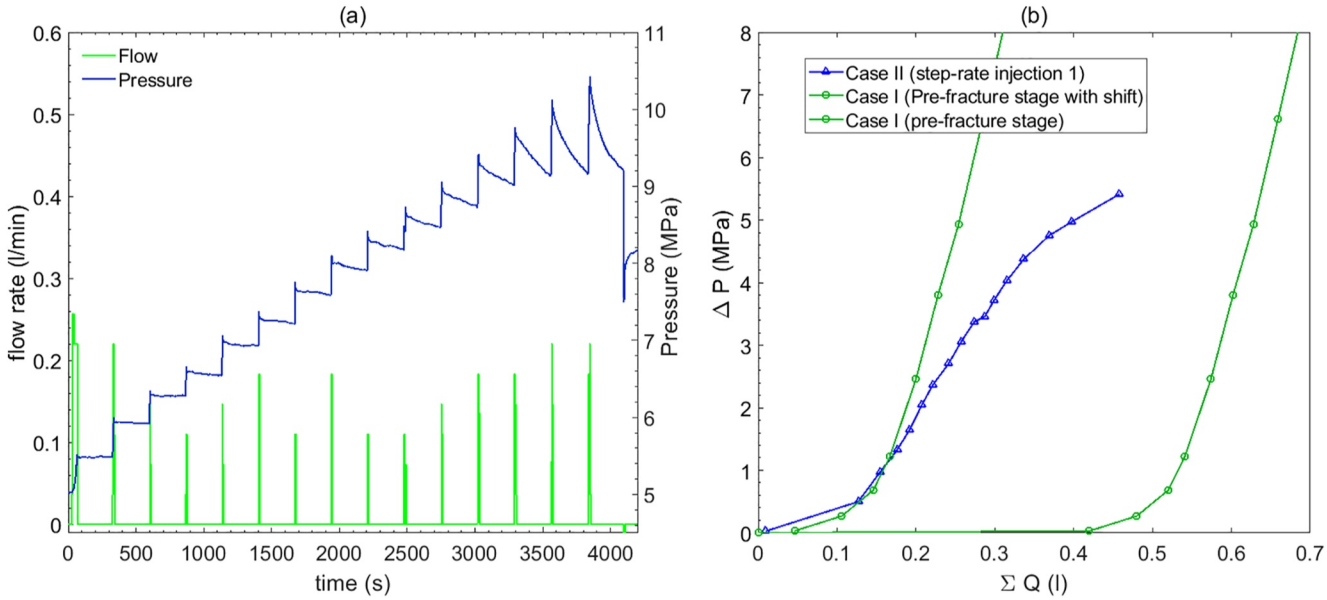

Figure 8. (a) Time of pressure and flow rate up to 4,100 s, and (b) Plot of accumulated injected volume versus pressure change for the two injection stages for the step-rate injection method for fracture in-situ properties test in the section with a non-conductive fracture (Case II).

The d_{f3} represents the effective permeability of the flow domain beyond Fracture 2. The third "effective" fracture aperture (d_{f3}) does not change the simulated pressures if its value is larger than 5 μm.

5.2. Study of the Section With a Non-Conductive Fracture (Case II)

The section with a non-conductive fracture is located at a depth of 515.1 m and was identified using previously conducted detailed core and borehole characterization studies and acoustic televiewer and gamma logging (see Wenning et al., 2017, Table S4). This fracture was not found to be conductive based on the FFEC logging analysis (Doughty et al., 2017; Tsang et al., 2016) and is thus considered to be a closed fracture. The Case II SIMFIP test was conducted on this fracture. The time evolution of pressure and injection flow rate is shown in Figure 2b. The test was conducted with a number of injection pulses up to 4,100 s. In this work, this period of the test is analyzed using conceptual model 3 with the assumption that Fracture 2 (see Figure 3) is initially closed. The time variation of the measured pressure shows some similarity with the step-wise increase of pressure in Case I (section with no fracture) up to 1,400 s. After 1,400 s (or after an increase of pressure ΔP by about 2 MPa), the measured pressure shows a "jump and then decreasing" behavior during the rest periods after an injection pulse (Figure 8a). This can be explained by water leakage from Fractures 1 and 2 to the fracture network domain represented by Fracture 3. when the closed fracture opened up. This is also reflected in Figure 8b in the plot of pressure change versus accumulated injected volume ($\sum Q$), which displays a smaller slope after ΔP has reached about 2 MPa in this case than in Injection 2 of Case I (Figure 8b). In addition, this plot shows some similarities between Injection 2 of Case I for injection volumes lower than 0.15 l (Figures 4 and 8b). This can explain the constant pressure increase at early water injection steps, that is, when the system is closed. Note that in Figure 8b, the wellbore storativity function for the packed-off section from Case I is used from the pre-fracturing stage but with a 0.37 l shift in the accumulated injection volume.

The best-fitting model result, along with the measured pressure up to about 4,100 s, is shown in Figure 9. For the first five injection steps, a single fracture model based on conceptual model 3 (with $d_{f2} = 0$, which means the second fracture is a closed fracture) provides good agreement, with fracture parameters d_{f1} of 25 μm and L_{f1} of 2.55 m. To maintain a good fit with the later steps, from the time of 1,400 s, the narrow section [Fracture 3] needs to be opened with a non-zero aperture d_{f2}, and thus this is no longer a closed fracture. This occurs at a pressure of 7.4 MPa, much lower than the fracturing pressure found in the analysis of Case I data. The best modeling results for Fracture 2 parameters are d_{f2} of 0.75 μm and L_{f2} of 1.00 m. Note that the

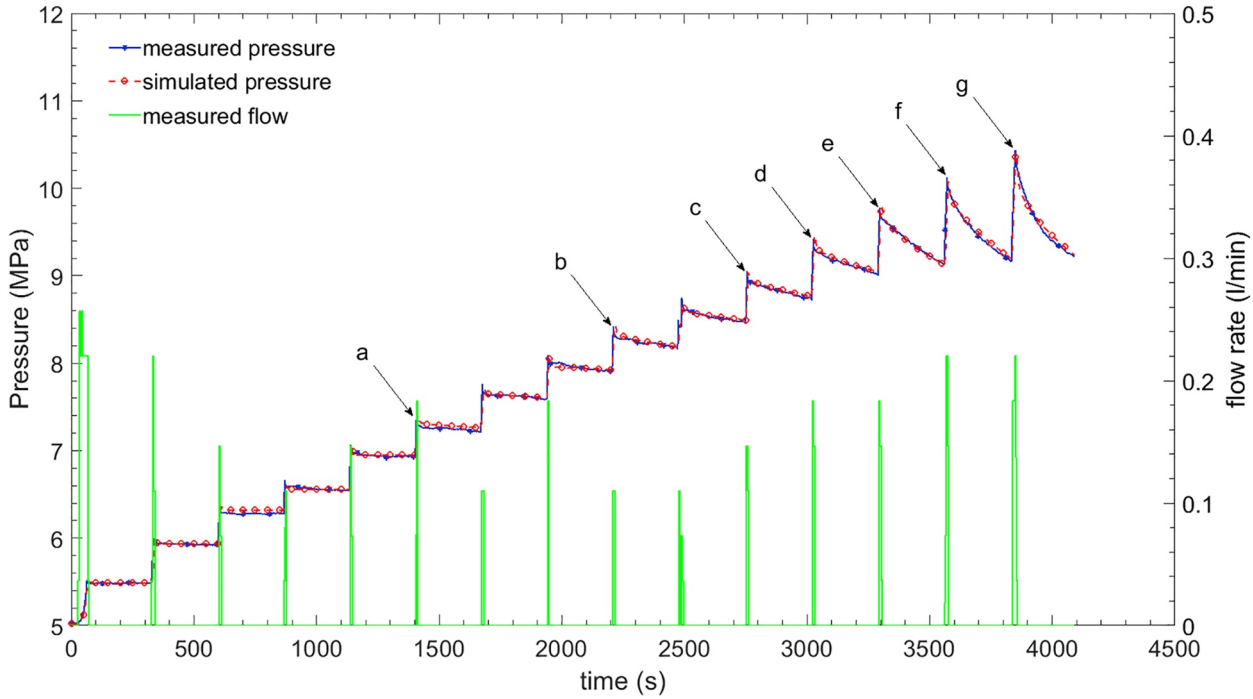

Figure 9. Time of the modeled pressure and measured pressure in the packed-off section during the step-rate injection method for fracture in-situ properties test in section with a non-conductive fracture (Case II). The arrows show the time and pressure where the model parameters are changed.

total radius of fractures ($L_{f1} + L_{f2}$) is assumed to be set to 3.55 m. In addition, the best model shows that the aperture of Fracture 1 ($d_{f1} = 25$ μm) remains unchanged during the step-rate injection. Figures 10a and 10b show the variation with time and with maximum pressure at each injection step for the two parameters d_{f2} and L_{f1}. The variation with time shows that the L_{f1} value increases from 2.55 m at 2,300 s to 3.0 m at 3,800 s. Similarly, the variation with a maximum pressure of L_{f1} shows that it increases more at larger pressure (Figure 10b). The variation with time and pressure of d_{f2} shows that it increases earlier and at lower pressure compared to L_{f1}. The d_{f2} increases at 7.4 MPa linearly, with L_{f1} starting to increase at 8.4 MPa. These results show directly from field data the coupled hydromechanical effect operating in this test.

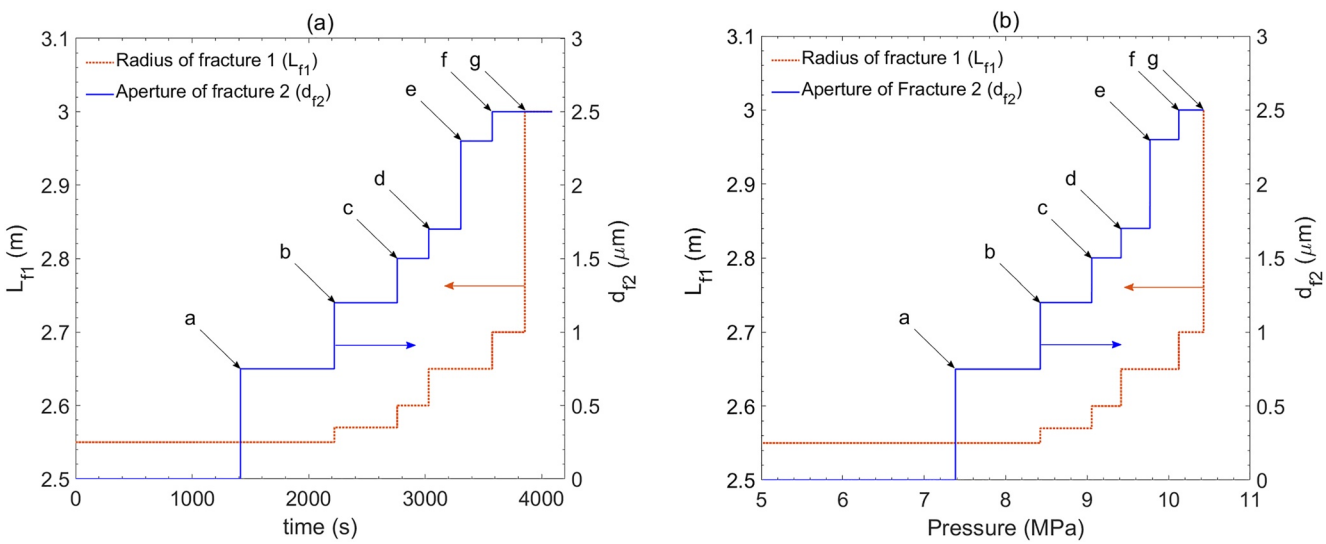

Figure 10. Modeling results for Case II, (a) The maximum pressure by each injection step, and (b) Time versus aperture of Fracture 2 (d_{f2}) and radius of Fracture 1 (L_{f1}). (Note that arrows show the *y*-axes for each curve).

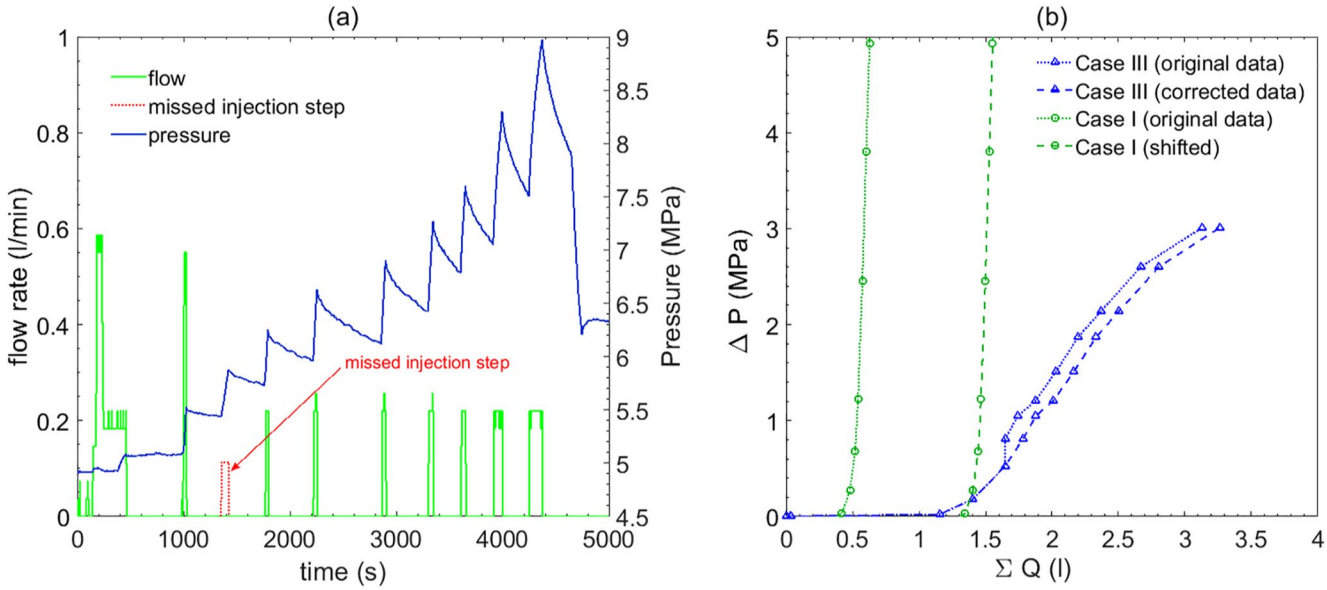

Figure 11. (a) Time of the injected flow rate (left *y*-axes) and pressure, and (b) Plot of accumulated injected volume versus pressure change in the packed-off section during the step-rate injection method for fracture in-situ properties test in section with a conductive fracture (Case III).

5.3. Study of the Section With a Conductive Fracture (Case III)

To model the case with an initially conductive fracture, conceptual model 3 is also used (see Figure 3). The time evolution of measured pressure and injection flow rate is presented in Figure 2c. Our study so far looks only at the first part of the injection up to 4,650 s (Figure 11a). The plot of accumulated injected flow volume ($\sum Q$) versus pressure change has a lower slope in this test than in Case I and Case II (Figure 11b). This is because the presence of a flowing fracture causes the section to have a lower stiffness. Note that the storativity of the packed-off section of the borehole from the pre-fracturing stage in Case I is still used in the modeling of this case with a 0.925 l shift in accumulated injection volume. The flow rate of one of the injection steps, at the time 1,350 s, was missed on the data set from the field test. This missed injection step results in a sudden jump in the plot of accumulated injection volume versus pressure (Figure 11b). The missed injection flow is estimated from Figure 11b to be about 0.14 l (by ensuring a smooth curve without the sudden jump), and the updated accumulative injection volume is plotted along with the original data.

The best-fitting model result, along with the measured pressure, is shown in Figure 12. The modeled pressure shows that the first seven injection steps can be matched with the good agreement without changing the parameters. However, in order to have a good agreement between the modeled and the measured pressure above 8.0 MPa, the parameter L_{f1} has to be increased from 7.55 to 7.9 m. It is interesting to note that a change in Fracture 1 parameters was also seen in Case II at a similar pressure value (7.4 MPa). Note that it was assumed the total radius of $L_{f1} + L_{f2}$ remains unchanged so that, as the radius L_{f1} is increased, the L_{f2} is reduced accordingly. The estimated transmissivity of the conductive fractures using the estimated fractures' parameters is 0.8–1.5 $\times 10^{-9}$ m^2/s. It is of interest to note that these estimated fracture transmissivity values are in the range of 2×10^{-10} m^2/s to 4×10^{-9} m^2/s, estimated by Doughty et al. (2017) for this interval using the FFEC logging method.

5.4. The Effect of Fracture Storativity

In all the cases studied above, the specific storage of the fracture is an important but unknown parameter. Rutqvist et al. (1998) estimated the in-situ storativity of fractured rocks in similar regions in Sweden by using high pressure injection field testing. Their results indicated a decreasing storativity with an increase of effective stress and depth. Besides varying with stress, storativity can also be affected by filling materials, which may have a lower stiffness. The specific storage of a fracture is also linked to the aperture and size of the fracture opening, which is contingent on the combined stiffness of the fracture and the ambient rock

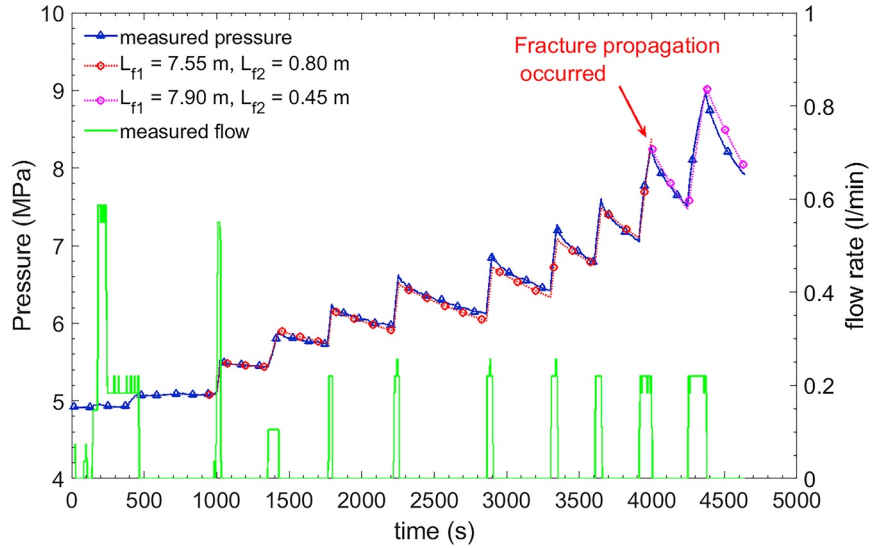

Figure 12. Plot of modeled pressure and measured pressure as a function of time in the packed-off section with a conductive fracture (Case III).

mass (Rutqvist et al., 1998). Figure 13 summarizes the results of field data from several sites in Sweden (Rutqvist et al., 1998), and it shows that the storativity of fractures at different depths can vary by an order of magnitude. In the present work, it is assumed to be equal to 1×10^{-8}, corresponding to values at similar depths in Figure 13.

To explore the sensitivity of the results to this parameter, the modeling of all three cases was repeated for two additional values of storage capacity by increasing and decreasing it by an order of magnitude. Table 1 shows the best-fit fracture parameters for different fracture storage coefficients for these three cases. The results generally show that the volume of fractures increases about 10 times with a reduction of the fracture storativity on the order of 10 times. Further studies are needed to determine field estimates of this parameter.

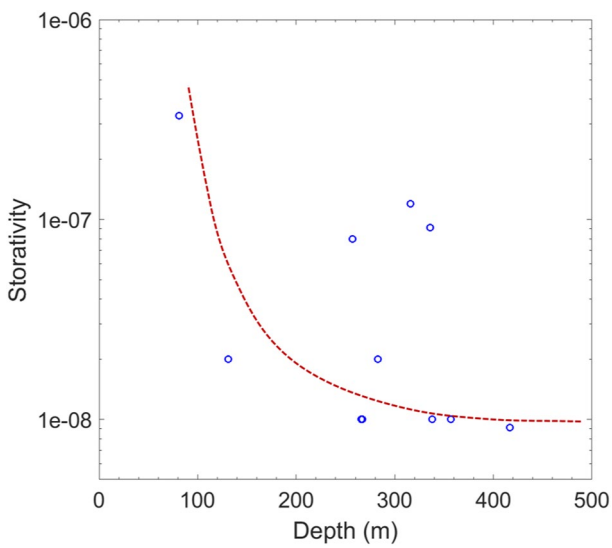

Figure 13. Depth versus fracture storativity measured by high-pressure testing (data are taken from Rutqvist et al., (1998)).

5.5. Results From Supplementary Study With a Coupled Hydromechanical Model

As mentioned in Section 4.2, as a supplement to our main analysis and for comparison with results from the simple hydraulic model, a coupled hydromechanical model was developed and applied to one example, which is the set of Case I data for the time period after the fracture has been induced by fluid injection. This particular data set represents the following situation. Under constant injection, the pressure in the borehole section with intact rock is increased until it reached a value (15.5 MPa from the field data) which exceeded the tensile strength of the rock, and a new fracture was created. This was evidenced by a sudden drop in pressure data as flow leaks into the new fracture. The injection was continued for another 40 s and then stopped with the result that pressure decreased with the time displayed a change in slope at this point (see Figure 14).

To simulate the pressure behavior, the coupled HM model presented in Section 4.2 and Appendix was used, together with the required values of parameters as shown in Table 2. Many of the parameter values are not known for this site, but some work is currently ongoing to estimate some of them. In our HM model, typical or estimated values were used, together with sensitivity studies on some of the more sensitive parameters.

Table 1
Parameters for Best Model for Different Fracture Storativity

Test	$Sf = 1 \times 10^{-7}$	$Sf = 1 \times 10^{-8}$	$Sf = 1 \times 10^{-9}$
Case I	$d_{f1} = 11.7$ μm, $L_{f1} = 0.75$ m	$d_{f1} = 13.5$ μm, $L_{f1} = 2.5$ m	$d_{f1} = 15$ μm, $L_{f1} = 7.8$ m
	$d_{f2} = 2.3$ μm, $L_{f2} = 0.25$ m	$d_{f2} = 2.3$ μm, $L_{f2} = 0.8$ m	$d_{f2} = 2.3$ μm, $L_{f2} = 2.0$ m
	$V_f = 2.38 \times 10^{-5}$ m^3	$V_f = 2.99 \times 10^{-4}$ m^3	$V_f = 3.12 \times 10^{-3}$ m^3
Case II	$d_{f1} = 25$ μm,	$d_{f1} = 25$ μm,	$d_{f1} = 25$ μm,
	$L_{f1} = 0.8/0.95$ m,	$L_{f1} = 2.55/3.0$ m,	$L_{f1} = 8.1$ m,
	$d_{f2} = 0.6/2.95$ μm,	$d_{f2} = 0.75/2.5$ μm,	$d_{f2} = 0.1/0.6$ μm,
	$L_{f2} = 1.0/0.85$ m	$L_{f2} = 1.0/0.55$ m	$L_{f2} = 1.0$ m
	$V_f = 5.25/9.25 \times 10^{-5}$ m^3	$V_f = 5.25/7.35 \times 10^{-4}$ m^3	$V_f = 5.16/5.18 \times 10^{-3}$ m^3
Case III	$d_{f1} = 75$ μm,	$d_{f1} = 75$ μm,	$d_{f1} = 75$ μm,
	$L_{f1} = 2.4/2.55$ m,	$L_{f1} = 7.55/7.9$ m,	$L_{f1} = 24.7/24.9$ m,
	$d_{f2} = 3.2/3.4$ μm,	$d_{f2} = 3.0$ μm,	$d_{f2} = 2.5/3.0$ μm,
	$L_{f2} = 0.35/0.2$ m	$L_{f2} = 0.8/0.35$ m	$L_{f2} = 1.2/1.0$ m
	$V_f = 1.38/1.54 \times 10^{-3}$ m^3	$V_f = 1.36/1.48 \times 10^{-2}$ m^3	$V_f = 1.44/1.46 \times 10^{-1}$ m^3

The right-hand column of Table 2 shows the range of parameters explored in one-at-a-time sensitivity studies and parameters shown with a single value without a range are those where the values are either relatively well-known and of less sensitivity. Among this list of parameter values, the horizontal (σ_1) and vertical stresses (σ_3), are suggested in an initial estimation provided by Guglielmi, Cook, Soom, Dobson, et al. (2021), and then sensitivity analysis was made by giving them a range as shown. The results of model simulations indicate that the elastic modulus of the rock, the horizontal stress, the fracture radius, its initial aperture, and the normal fracture stiffness of the fracture are the parameters that play the most important roles in a successful fitting of pressure data (Figure 14). Figure 15 shows a case of good data fit, which can be obtained by using a set of parameter values shown in the middle column of Table 2. This set of "best-fitting" parameters indicate a fracture length of 2.3 m with an initial aperture of 13 μm with a normal fracture stiffness of 800 GPa/m, which corresponds to a storativity value of 1.2×10^{-8} using Equation 11. These results are very close to the best-fitting results of the hydraulic model for Case I, shown in Table 1, for the base-case storativity value of $S_f = 10^{-8}$. Thus, good agreement has been found between the hydraulic and HM analyses.

It has to be noted that data fitting with the coupled HM model is not unique and it is sensitive not only to the fracture aperture and radius, but also to the assumed values of rock elastic modulus, local horizontal stresses, and normal fracture stiffness, whose values are uncertain for the site at the tested borehole interval. Typical ranges of these parameters from the literature are very large. For example, the range of values for fracture normal stiffness can be 100–1,100 GPa/m for granitic rocks (Zangerl et al., 2008).

Not only was sensitivity analysis to parameter values performed, but the effect of different hydromechanical boundary conditions in the hydromechanical model was also investigated. For this, four scenarios were considered: Scenario 1: top boundary free, right side fixed deformation in radial directions with initial lateral load; Scenario 2: top free, side fixed, without right boundary load; Scenario 3: all boundaries free; Scenario 4: all boundaries closed. The differences among the best matching results for these four scenarios in terms of fracture aperture and radius are within 10%.

6. Discussion and Conclusion

We have presented a primarily hydraulic model analysis of flow and pressure data at different stages of fracturing and fracture opening/propagation during a coupled HM field experiment. The experiment was carried out using the SIMFIP probe at a depth of about 500 m in the COSC-1 deep borehole in the crystalline rock near Åre, Sweden. The objective has been to identify fluid injection-induced fracturing and changes in fracture geometry at different time stages of the experiments based on flow and pressure data (Cases

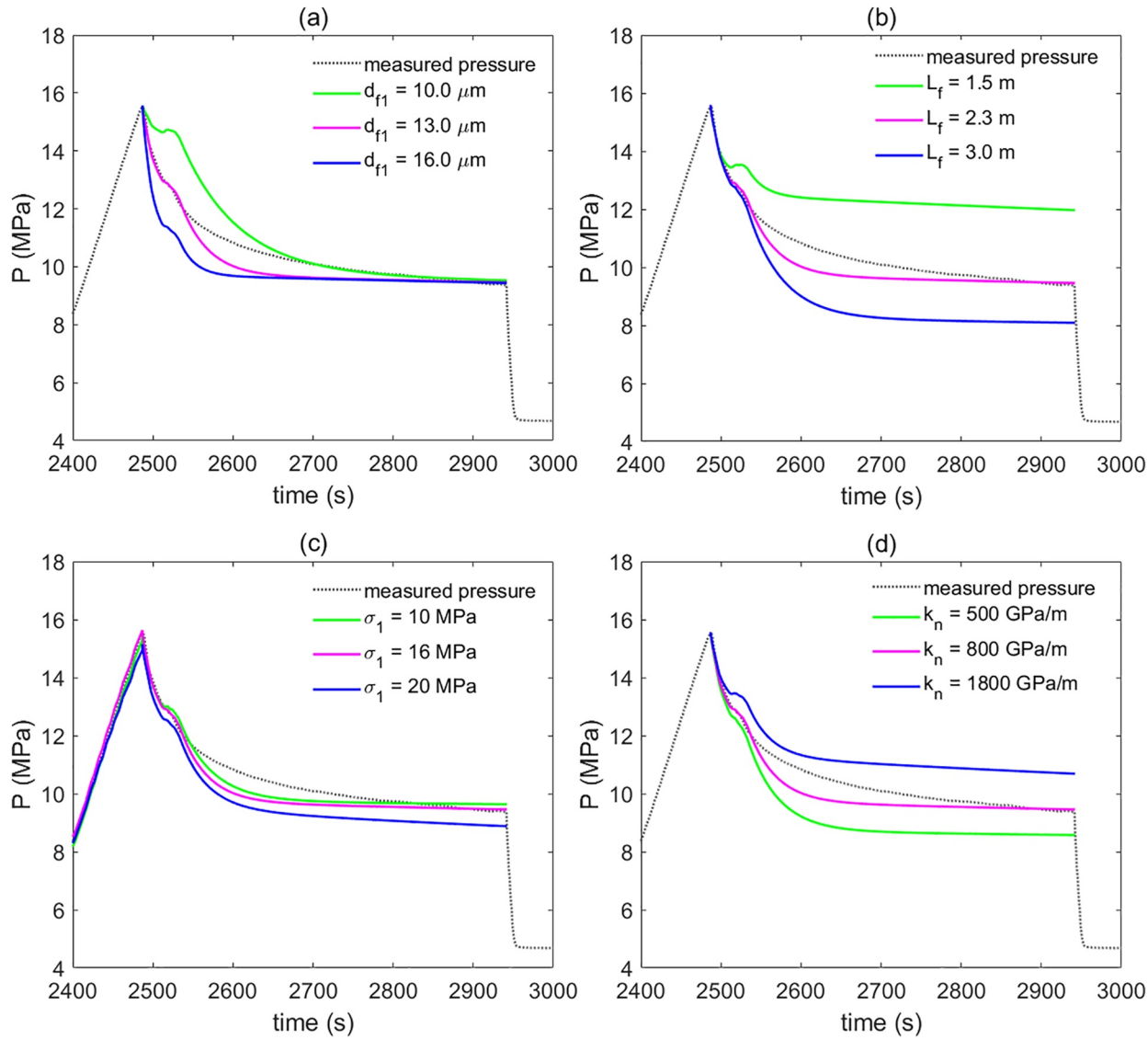

Figure 14. Effect of changes in the essential hydromechanical parameters on pressure variation with time, (a) Initial fracture aperture; (b) Fracture length; (c) Initial horizontal stress σ_1; (d) Normal fracture stiffness.

1–3, Figure 1) by applying a simple fracture flow model to each of a series of time stages of the experiment. The geometry of the fracture (aperture and radius) is allowed to change from one time stage to the next as required by the field data, but it is constant within each time stage. In this way, the HM behavior of fluid injection-induced fracture changes can be obtained directly from the field data as a function of time. As a supporting analysis, we have also carried out a coupled HM model analysis for one of the cases, to provide a comparison with the simpler hydraulic model as well as to provide insights concerning the interlinkage between the two approaches. A topic of interest between the two approaches is how the storage term, fracture storativity in the hydraulic model, and the fracture normal stiffness in the HM model, are considered and what is the impact and related uncertainty.

For the test section with no initial fracture (Case I), the data for times before the creation of the injection-induced fracture were used to derive the pressure response characteristics of the packed-off borehole section. The effective storativity of this system, including the borehole, the packers, the SIMFIP probe, and tubing, was used for the analysis of all three cases. Pressure data in Case I show very definitely that a fracture was induced when the pressure reaches a value of 15.5 MPa, which is in the range of typical values for the tensile

Table 2
Hydromechanical Parameters Used in the Model

	Parameters	Best fit	Range of each parameter used in the sensitivity analysis
Intact rock	Porosity $\phi(-)$	0.01	0.02
	Permeability (m^2)	2e−21	2e−21
	Elastic modulus (GPa)	30	15–45
	Poisson's ratio $(-)$	0.3	0.1–0.3
	Rock density (kg / m^3)	2,800	2,800
Fractures	Porosity ϕ_F	0.9	0.1–0.9
	Initial aperture d_f (μm)	13	8–20
	Fracture length L_f (m)	2.3	1.5–3.0
	Elastic modulus E_F (GPa)	5	5–20
	Poisson's ratio ν_F $(-)$	0.2	0.1–0.3
	Fracture normal stiffness k_n (GPa / m)	800	100–1,800
	Horizontal stress σ_1 (MPa)	16	10–20
	Horizontal stress σ_2 (MPa)	15.7	15.7
	Vertical stress σ_3 (MPa)	13.8	7.5–20

strength of crystalline rock. The induced fracture is then studied with three different conceptual models as presented in Figure 3 and the results show that the conceptual model that best captures the measured pressure behavior is Model 3, consisting of a single fracture that connects to a continuum fracture network through a narrow fracture (fracture with a smaller hydraulic aperture than the primary fracture; Figure 6).

A parameter sensitivity analysis shows the importance of continuing the injection for a short time period after the creation of the fracture, in order to be able to determine more accurately the aperture of the induced fracture d_{f1}. This should be a point of consideration for future field tests. The parameter sensitivity study also shows that the end-point pressure at the recovery stage after the injection is stopped provides information on the fractured radius. Therefore, the continuation of the recovery period to a steady pressure can help to determine the length of the induced fracture (L_{f1}). If the pressure drops to the (initial) hydrostatic pressure, it means that the fracture is conductive and connected to a large (regional) network of conductive fractures. Regarding the smaller aperture fracture beyond the induced fracture (Fracture 2), its aperture is related to a leak-off process. A sensitivity analysis shows that the aperture (d_{f2}) of this fracture controls the rate of the pressure drop. The aperture (conductivity) of the far-field fracture network or continuum fractured rock domain (represented by d_{f3}) beyond the induced fracture is found not to affect the pressure profile as long as its value is larger than that of the connecting narrow fracture (d_{f2}).

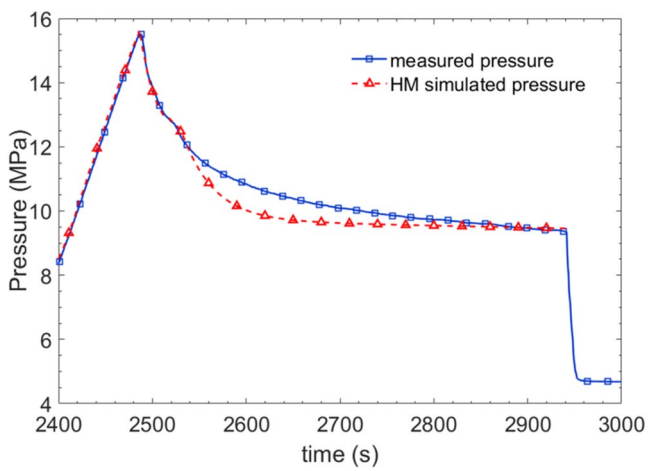

Figure 15. Measured and the simulated pressure from the hydromechanical model in section with an induced fracture (Case I). The model parameters for the best fit are provided in Table 2.

In the case of the initially non-conductive fracture (Case II), the pressure response shows that the fracture has a limited radius and with no sign of leak-off up to 7.3 MPa (with the ambient pressure $P_0 = 5.02$ MPa). Thus, the pressure increases after each injection pulse become steady shortly after each pulse (a step up). However, at a pressure of 7.3 MPa and above, the pressure step decreases after each injection pulse. This can be explained by the introduction of a narrow fracture beyond Fracture 1, to capture the leak-off effect. After this point, the fracture properties, aperture of the narrow fracture (d_{f2}), and/or radius of the main fracture (L_{f1}) need to be changed with subsequent injection pulses in order to match

the field data (see Figure 10). The slope of the pressure drops in between two injection pulses is related to leak-off over the time between the two pulses, and hence related to the conductivity of the narrow fracture (d_{f2}) as well as the radius of the main fracture (L_{f1}).

In the case of the initially conductive fracture (Case III), the changes in fracture geometry are very small with the injection of water pulses, because the volume of the initial fracture system is already large enough and is connected to a domain of fracture network for water to leak-off. However, when the pressure reaches about 8.2 MPa ($P_0 = 4.92$ MPa), the volume of a fracture needs to be increased by about 10% to maintain a good match with the pressure data. This is much smaller than the non-conductive fracture case (Case II), where the volume of the fractures needs a 50% increase.

One of the main challenges in this analysis is the uncertainty related to fracture storativity (S_f), which cannot be independently determined. In order to understand its effect on the results, two additional storativity values of 1×10^{-7} and 1×10^{-9} were also considered, one order of magnitude above and below the best-estimate initial value of 1×10^{-8}, which is based on the study of field data from similar crystalline rock sites in Sweden (Rutqvist et al., 1998). The results show that the estimated volume of the fractures (combined result of fracture aperture and radius) is inversely related to the storativity of the fracture. So, as the storativity of the fracture is increased ten-fold, the volume of the fractures required to fit the field data is 10 times less.

The results of the full hydromechanical coupled model for one of the test cases show that fitting of pressure data is sensitively controlled not only by fracture aperture and radius but also by rock elastic modulus, normal fracture stiffness, and local stresses. Many of the values of these mechanical parameters are not available at the site near the testing borehole interval, and typical values for crystalline rock in the literature have a large range. Thus, there are considerable uncertainties in the results from the coupled HM model. Nevertheless, coupled HM modeling was conducted with a set of reasonable parameter values within their typical ranges, and the comparison shows that the estimated best-fitting fracture aperture, length, and storage parameter from the hydraulic and HM analyses are similar, indicating that the simpler hydraulic analysis can indeed yield valuable first-order information concerning the generated/propagated fracture properties.

In conclusion, the present study does not claim that the derived geometric parameters of the induced fractures or their changes are unique. They represent only a set of results that are consistent with the field data. However, a number of sensitivity analyses were performed to give a feeling of possible ranges. Further, data analysis indicates that in the field it is very useful to continue the injection for a short time period after the creation of a fracture, as indicated by a sudden pressure drop. This part of the pressure data can be used to pin down more accurately the hydraulic aperture of the induced fracture near the borehole.

The study also shows that the pressure required for fracturing at the depth of about 500 m in crystalline rock at the site (Case I) is 15.5 MPa, while the pressure required for opening of an initially non-conducting fracture is about 7.2 MPa (Case II), and the pressure to open up a conducting fracture is estimated to be 8.2 MPa. In other words, in Case I, a mode-1 tensile fracture was created as the pressure was observed to drop suddenly as injection pressure reached a critical value of 15.5 MPa, whereas in Cases II and III, injection pressure started to open up an initially non-conducting fracture (Case II) and conducting fracture (Case III) after pressure reached a fracture opening pressure value in the range of 7.2–8.2 MPa.

This work was able to arrive at some significant conclusions, which include (a) successful understanding of data in the three different cases for pressure values both below fracture opening pressure and above it, (b) determination of the non-linear compressibility of the borehole section bracketed by packers, with the identification of initial "dead" injection volume with no pressure change, (c) determination of the non-linear relationship between fracture aperture with pressure for values above the fracture opening pressure, and (d) confirmation that the simple conceptual model using a time-stage approach may be adequate in understanding field data. We believe that these conclusions provide useful insight for a further fully coupled hydromechanical analysis of flow and pressure, as well as borehole deformation data from this unique field test conducted at ~500 m in the COSC-1 borehole.

Appendix: Coupled Hydromechanical Model

The mathematical model describing the coupled hydromechanical processes follows the implementation of Zhou et al. (2021). This model does not account for shear deformation of the fracture, which may be acceptable when applied to a new injection-induced fracture in intact rock (Case I in the present study). The fluid flow in the subsurface porous media is described by Darcy's law, similar to the hydraulic model.

$$u_w = -\frac{K}{\mu}\left(\nabla p - \rho \mathbf{g}\right) \tag{A1}$$

The mass conservation equation is formulated:

$$\frac{\partial \rho \phi}{\partial t} - \nabla \cdot \rho \frac{K}{\mu}\left(\nabla p - \rho \mathbf{g}\right) + Q = 0 \tag{A2}$$

$$\frac{\partial \rho \phi}{\partial t} = \rho S \frac{\partial p}{\partial t} \tag{A3}$$

The storage term is expressed:

$$S = \phi X_f + \left(1 - \phi\right) X_m \tag{A4}$$

where ϕ is the initial porosity assumed to be homogeneously distributed, and X_f and X_m are the compressibility of the fluid that is, water, and of surrounding matrix, respectively.

The storativity of the fracture is expressed using:

$$S_f = \rho \mathbf{g}\left(X_f d_f + \frac{\partial d_f}{\partial p}\right) \tag{A5}$$

The storativity can be related to the normal stiffness, k_n of the fracture as described by Rutqvist et al. (1998):

$$S_f = \rho \mathbf{g}\left(X_f d_f + \frac{1}{k_n}\right) \tag{A6}$$

The deformation of the rock and fracture is assumed to be elastic. The force balance equation is given by Equation A7:

$$\nabla \sigma + F_v = 0 \tag{A7}$$

where F_v is the external force, including the gravitational forces, σ is the stress tensor acting on the matrix. According to Rutqvist et al., (2002, 2013), the stress-induced mechanical porosity ϕ_{eff} can be expressed by stationary initial porosity ϕ and the volumetric strain ϵ_v:

$$\phi_{\text{eff}} = 1 - \left(1 - \phi\right) e^{-\epsilon_v} \tag{A8}$$

with the volumetric strain being the sum of the axial strain, according to Hook's law and the theory of poroelasticity:

$$\epsilon_{ii} = \frac{1}{E}\left[\sigma'_{ii} - \nu\left(\sigma'_{jj} + \sigma'_{kk}\right)\right] i,j,k = x,y,z \tag{A9}$$

$$\sigma'_{ii} = \sigma_{ii} - \alpha_b\left(p - p_{ref}\right) \tag{A10}$$

where E is the elastic modulus, ν is the Poisson's ratio, σ'_{ii} the effective stress in the porous medium, σ_{ii} is the external stress acting on the matrix, α_b is the biot-coefficient, p is the pore pressure, and p_{ref} is the stationary reference pressure. To obtain the effective permeability of surrounding rocks, an empirical relationship between the permeability and porosity has been generally applied (Li et al., 2016; Pan & Connell, 2007; Pashin, 1998; Rutqvist et al., 2002):

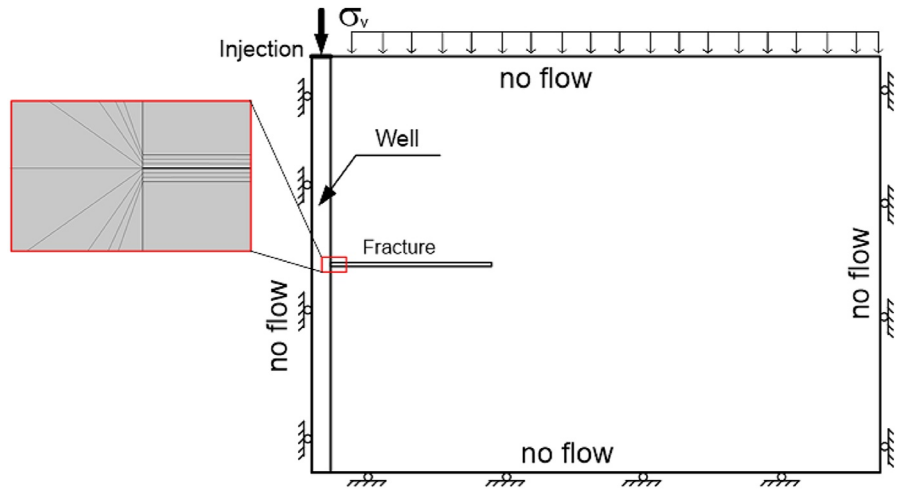

Figure A1. Boundary conditions and simulation domain with the left boundary being the axis of symmetry. Zoom into the finite element discretization of the equidimensional fracture.

$$K_{\text{eff}} = K \cdot \exp\left(\frac{\phi_{\text{eff}}}{\phi}\right)^n \tag{A11}$$

The permeability of the fracture can be related to the intrinsic permeability using the cubic law

$$k_f = \frac{d_f^2}{12} \tag{A12}$$

The simulation model is designed to be similar to the hydraulic model but implemented for the hydro-mechanical (HM) context, that is, mechanical parameters and boundary conditions are specified as well. The model is radially symmetric. Spatial discretization is based on the finite element method, where the fracture elements have the same dimensionality as the surrounding matrix. The HM simulation domain has the same size as the hydraulic model with the same hydraulic boundary conditions. The left boundary is the axial symmetry, and the top is set a Neumann boundary condition to specify the injection rates. All other boundaries are assumed to be no-flow. The fracture is assumed to be horizontal and has a rectangular cross-section with a constant aperture (Figure A1).

Data Availability Statement

The field data is openly available in a data repository (Zenodo): https://doi.org/10.5281/zenodo.5171638.

Acknowledgments
The authors gratefully acknowledge the financial support from the Geological Survey of Sweden (SGU research contract 36-2025-2018) with Uppsala University, and the Spent Fuel and Waste Disposition Science and Technology Campaign, Office of Nuclear Energy, of the U.S. Department of Energy (Contract Number DE-AC02-05CH11231) with Lawrence Berkeley National Laboratory. The authors also thank Henning Lorenz, Jan-Erik Rosberg, Emil Lundberg, Georgios Niachros, Niranjan Joshi, Bjarne Almqvist, Eduardo Reynolds, and Roland Roberts, who participated in the 2019 field campaign. The authors would like to thank anonymous reviewers for their constructive comments.

References

Amann, F., Gischig, V., Evans, K., Doetsch, J., Jalali, R., Valley, B., et al. (2018). The seismo-hydromechanical behavior during deep geothermal reservoir stimulations: Open questions tackled in a decameter-scale in situ stimulation experiment. *Solid Earth*, *9*, 115–137. https://doi.org/10.5194/se-9-115-2018

Cao, C., Xu, Z., Chai, J., Qin, Y., & Tan, R. (2018). Mechanical and hydraulic behaviors in a single fracture with asperities crushed during shear. *International Journal of Geomechanics*, *18*, 04018148. https://doi.org/10.1061/(ASCE)GM.1943-5622.0001277

Cappa, F., Guglielmi, Y., Rutqvist, J., Tsang, C.-F., & Thoraval, A. (2008). Estimation of fracture flow parameters through numerical analysis of hydromechanical pressure pulses. *Water Resources Research*, *44*, W11408. https://doi.org/10.1029/2008WR007015

COMSOL Multiphysics® v. 5.4. COMSOL AB. Retrieved from www.comsol.com

De Barros, L., Daniel, G., Guglielmi, Y., Rivet, D., Caron, H., Payre, X., et al. (2016). Fault structure, stress, or pressure control of the seismicity in shale? Insights from a controlled experiment of fluid-induced fault reactivation. *Journal of Geophysical Research: Solid Earth*, *121*, 4506–4522. https://doi.org/10.1002/2015JB012633

Derode, B., Guglielmi, Y., De Barros, L., & Cappa, F. (2015). Seismic responses to fluid pressure perturbations in a slipping fault. *Geophysical Research Letters*, *42*, 3197–3203. https://doi.org/10.1002/2015GL063671

Dessirier, B., Tsang, C.-F., Hedayati, M., Lorenz, H., Juhlin, C., & Niemi, A. (2021). *A study of correlations of geophysical and geochemical logs with hydrogeological features in a 2.5-km deep borehole in crystalline rock (manuscript under preparation).*

Domenico, P. A., & Schwartz, F. W. (1998). *Physical and chemical hydrogeology*. Wiley.

Doughty, C., Tsang, C.-F., Rosberg, J.-E., Juhlin, C., Dobson, P. F., & Birkholzer, J. T. (2017). Flowing fluid electrical conductivity logging of a deep borehole during and following drilling: Estimation of transmissivity, water salinity and hydraulic head of conductive zones. *Hydrogeology Journal*, *25*, 501–517. https://doi.org/10.1007/s10040-016-1497-5

Duboeuf, L., De Barros, L., Cappa, F., Guglielmi, Y., Deschamps, A., & Seguy, S. (2017). Aseismic motions drive a sparse seismicity during fluid injections into a fractured zone in a carbonate reservoir. *Journal of Geophysical Research: Solid Earth*, *122*, 8285–8304. https://doi.org/10.1002/2017JB014535

Dutler, N., Valley, B., Gischig, V., Viller, L., Krietsch, H., Doetsch, J., et al. (2019). Hydraulic fracture propagation in a heterogeneous stress field in a crystalline rock mass. *Solid Earth*, *10*(6), 1877–1904. https://doi.org/10.5194/se-10-1877-2019

Follin, S. (2008). Bedrock hydrogeology Forsmark: site descriptive modeling. SDM-Site Forsmark. Retrieved from www.skb.com/publication/1877175

Follin, S., Hartley, L., Rhén, I., Jackson, P., Joyce, S., Roberts, D., & Swift, B. (2014). A methodology to constrain the parameters of a hydrogeological discrete fracture network model for sparsely fractured crystalline rock, exemplified by data from the proposed high-level nuclear waste repository site at Forsmark, Sweden. *Hydrogeology Journal*, *22*, 313–331. https://doi.org/10.1007/s10040-013-1080-2

Fu, P., Schoenball, M., Ajo-Franklin, J., Chai, C., Maceira, M., Morris, J. P., et al. (2021). Close observation of hydraulic fracturing at EGS collab experiment 1: Fracture trajectory, microseismic interpretations, and the role of natural fractures. *Journal of Geophysical Research: Solid Earth*, *126*, e2020JB020840. https://doi.org/10.1029/2020JB020840

Gee, D. G., Juhlin, C., Pascal, C., & Robinson, P. (2010). Collisional orogeny in the Scandinavian caledonides (COSC). *GFF*, *132*, 29–44. https://doi.org/10.1080/11035891003759188

Guglielmi, Y., Cappa, F., Avouac, J.-P., Henry, P., & Elsworth, D. (2015). Seismicity triggered by fluid injection-induced aseismic slip. *Science*, *348*, 1224–1226. https://doi.org/10.1126/science.aab0476

Guglielmi, Y., Cappa, F., Lançon, H., Janowczyk, J. B., Rutqvist, J., Tsang, C. F., & Wang, J. S. Y. (2014). ISRM suggested method for step-rate injection method for fracture in-situ properties (SIMFIP): Using a 3-components borehole deformation sensor. *Rock Mechanics and Rock Engineering*, *47*, 303–311. https://doi.org/10.1007/s00603-013-0517-1

Guglielmi, Y., Chang, C., Cook, P., Dobson, P., Soom, F., Nakagawa, S., et al. (2020). *Crystalline disposal R&D at LBNL: FY20 Progress Report*. Lawrence Berkeley National Lab. (LBNL).

Guglielmi, Y., Cook, P., Soom, F., Dobson, P., Kneafsey, T., Valley, B., et al. (2021). Estimating stress from three-dimensional borehole displacements induced by fluid injection in different types of fractured or faulted rocks. Presented at the Proceedings, 55th US Rock Mechanics/Geomechanics Symposium.

Guglielmi, Y., Cook, P., Soom, F., Schoenball, M., Dobson, P., & Kneafsey, T. (2021). In situ continuous monitoring of borehole displacements induced by Stimulated Hydrofracture Growth. *Geophysical Research Letters*, *48*, e2020GL090782. https://doi.org/10.1029/2020GL090782

Guglielmi, Y., Nussbaum, C., Jeanne, P., Rutqvist, J., Cappa, F., & Birkholzer, J. (2020). Complexity of fault rupture and fluid leakage in shale: Insights from a controlled fault activation experiment. *Journal of Geophysical Research: Solid Earth*, *125*, e2019JB017781. https://doi.org/10.1029/2019JB017781

Guglielmi, Y., Nussbaum, C., Rutqvist, J., Cappa, F., Jeanne, P., & Birkholzer, J. (2020). Estimating perturbed stress from 3-D borehole displacements induced by fluid injection in fractured or faulted shales. *Geophysical Journal International*, *221*, 1684–1695. https://doi.org/10.1093/gji/ggaa103

Hedin, P., Almqvist, B., Berthet, T., Juhlin, C., Buske, S., Simon, H., et al. (2016). 3D reflection seismic imaging at the 2.5 km deep COSC-1 scientific borehole, central Scandinavian Caledonides. *Tectonophysics*, *689*, 40–55. https://doi.org/10.1016/j.tecto.2015.12.013

Koyama, T., Neretnieks, I., & Jing, L. (2008). A numerical study on differences in using Navier–Stokes and Reynolds equations for modeling the fluid flow and particle transport in single rock fractures with shear. *International Journal of Rock Mechanics and Mining Sciences*, *45*, 1082–1101. https://doi.org/10.1016/j.ijrmms.2007.11.006

Li, S., Fan, C., Han, J., Luo, M., Yang, Z., & Bi, H. (2016). A fully coupled thermal-hydraulic-mechanical model with two-phase flow for coalbed methane extraction. *Journal of Natural Gas Science and Engineering*, *33*, 324–336. https://doi.org/10.1016/j.jngse.2016.05.032

López-Comino, J. A., Cesca, S., Heimann, S., Grigoli, F., Milkereit, C., Dahm, T., & Zang, A. (2017). Characterization of hydraulic fractures growth during the Aspö Hard Rock Laboratory experiment (Sweden). *Rock Mechanics and Rock Engineering*, *50*, 2985–3001. https://doi.org/10.1007/s00603-017-1285-0

Lorenz, H., Rosberg, J. E., Juhlin, C., Bjelm, L., Almqvist, B. S. G., Berthet, T., et al. (2015). COSC-1 – Drilling of a subduction-related allochthon in the Palaeozoic Caledonide orogen of Scandinavia. *Scientific Drilling*, *19*, 1–11. https://doi.org/10.5194/sd-19-1-2015

Niemi, A., Guglielmi, Y., Dobson, P., Paul, C., Chris, J., Chin-Fu, T., et al. (2021). *Coupled hydro-mechanical experiments on fractures in deep crystalline rock at COSC-1—field test procedures and first results (manuscript under preparation)*.

Pan, Z., & Connell, L. D. (2007). A theoretical model for gas adsorption induced coal swelling. *International Journal of Coal Geology*, *69*, 243–252. https://doi.org/10.1016/j.coal.2006.04.006

Pashin, J. (1998). Stratigraphy and structure of coalbed methane reservoirs in the United States: An overview. *International Journal of Coal Geology*, *35*, 209–240. https://doi.org/10.1016/s0166-5162(97)00013-x

Rhén, I., Forsmark, T., Hartley, L., Jackson, P., Roberts, D., Swan, D., & Gylling, B. (2008). *Hydrogeological conceptualisation and parameterisation: Site descriptive modeling SDM-site*. Retrieved from www.skb.com/publication/1967676/

Rutqvist, J., Leung, C., Hoch, A., Wang, Y., & Wang, Z. (2013). Linked multicontinuum and crack tensor approach for modeling of coupled geomechanics, fluid flow and transport in fractured rock. *International Journal of Rock Mechanics and Geotechnical Engineering*, *5*, 18–31. https://doi.org/10.1016/j.jrmge.2012.08.001

Rutqvist, J., Noorishad, J., Tsang, C.-F., & Stephansson, O. (1998). Determination of fracture storativity in hard rocks using high-pressure injection testing. *Water Resources Research*, *34*, 2551–2560. https://doi.org/10.1029/98WR01863

Rutqvist, J., Wu, Y.-S., Tsang, C.-F., & Bodvarsson, G. (2002). A modeling approach for analysis of coupled multiphase fluid flow, heat transfer, and deformation in fractured porous rock. *International Journal of Rock Mechanics and Mining Sciences*, *39*, 429–442. https://doi.org/10.1016/s1365-1609(02)00022-9

Theis, C. V. (1935). The relation between the lowering of the piezometric surface and the rate and duration of discharge of a well using groundwater storage. *Eos, Transactions American Geophysical Union*, *16*(2), 519–524. https://doi.org/10.1029/tr016i002p00519

Tsang, C.-F. (1991). Coupled hydromechanical-thermochemical processes in rock fractures. *Reviews of Geophysics*, *29*, 537–551. https://doi.org/10.1029/91RG01832

Tsang, C.-F., & Doughty, C. (2003). Multirate flowing fluid electric conductivity logging method. *Water Resources Research*, *39*(12), 1354–1362. https://doi.org/10.1029/2003WR002308

Tsang, C.-F., Hufschmied, P., & Hale, F. V. (1990). Determination of fracture inflow parameters with a borehole fluid conductivity logging method. *Water Resources Research*, *26*, 561–578. https://doi.org/10.1029/wr026i004p00561

Tsang, C.-F., & Niemi, A. (2013). Deep hydrogeology - A discussion of the issues and research needs. *Hydrogeology Journal*, *21*, 1687–1690. https://doi.org/10.1007/s10040-013-0989-9

Tsang, C.-F., Rosberg, J.-E., Sharma, P., Berthet, T., Juhlin, C., & Niemi, A. (2016). Hydrologic testing during drilling: Application of the flowing fluid electrical conductivity (FFEC) logging method to drilling of a deep borehole. *Hydrogeology Journal*, *24*, 1333–1341. https://doi.org/10.1007/s10040-016-1405-z

Tsang, C.-F., Rutqvist, J., & Min, K.-B. (2007). Fractured rock hydromechanics: From borehole testing to solute transport and CO_2 storage. *Geological Society, London, Special Publications*, *284*, 15–34. https://doi.org/10.1144/SP284.2

Wenning, Q. C., Berthet, T., Ask, M., Zappone, A., Rosberg, J.-E., & Almqvist, B. S. G. (2017). Image log analysis of in situ stress orientation, breakout growth, and natural geologic structures to 2.5 km depth in central Scandinavian Caledonides: Results from the COSC-1 borehole. *Journal of Geophysical Research: Solid Earth*, *122*, 3999–4019. https://doi.org/10.1002/2016jb013776

Witherspoon, P. A., Wang, J. S. Y., Iwai, K., & Gale, J. E. (1980). Validity of Cubic Law for fluid flow in a deformable rock fracture. *Water Resources Research*, *16*, 1016–1024. https://doi.org/10.1029/WR016i006p01016

Zang, A., Stephansson, O., Stenberg, L., Plenkers, K., Specht, S., Milkereit, C., et al. (2017). Hydraulic fracture monitoring in hard rock at 410 m depth with an advanced fluid-injectio protocol and extensive sensor array. *Geophysical Journal International*, *208*, 790–813. https://doi.org/10.1093/gji/ggw430

Zangerl, C., Evans, K. F., Eberhardt, E., & Loew, S. (2008). Normal stiffness of fractures in granitic rock: A compilation of laboratory and in-situ experiments. *International Journal of Rock Mechanics and Mining Sciences*, *45*(8), 1195–1210. https://doi.org/10.1016/j.ijrmms.2008.02.002

Zhou, D., Tatomir, A., & Sauter, M. (2021). Thermo-hydro-mechanical modelling study of heat extraction and flow processes in enhanced geothermal systems. In *Advances in geosciences* (Vol. *54*, pp. 229–240). Copernicus GmbH. https://doi.org/10.5194/adgeo-54-229-2021

Zimmerman, R. W., & Bodvarsson, G. S. (1996). Hydraulic conductivity of rock fractures. *Transport in Porous Media*, *23*, 1–30. https://doi.org/10.1007/BF00145263